

## DIMENSIONAL ROBUSTNESS AND INSTABILITY OF SHEARED, SEMIDILUTE, NANOROD DISPERSIONS\*

XIAOFENG YANG<sup>†</sup>, ZHENLU CUI<sup>‡</sup>, M. GREGORY FOREST<sup>§</sup>, QI WANG<sup>¶</sup>, AND  
JIE SHEN<sup>||</sup>

**Abstract.** Semidilute, nanorod dispersions interact nonlocally and nonlinearly through excluded-volume and distortional elasticity potentials. When driven by steady shear with confinement boundary conditions, remarkable rod orientational distribution behavior ensues: strong anisotropy; steady and unsteady responses; and gradient structure on (thus far) unpredictable lengthscales. Extreme variability and sensitivity of these features to experimental controls, coupled with nanorod measurement limitations, continue to confound materials processing strategies. Thus, modeling and simulation play a critical role. In this paper, we present a hierarchy of zero-dimensional (0-d), one-dimensional (1-d), and two-dimensional (2-d) physical space simulations of steady parallel-plate shear experiments using a mesoscopic tensor model for the rod orientational distribution [E. H. MacMillan, *A Theory of Anisotropic Fluid*, Ph.D. thesis, Department of Mechanics, University of Minnesota, Minneapolis, MN, 1987, Z. Cui and Q. Wang, *J. Non-Newtonian Fluid Mech.*, 138 (2006), pp. 44–61] and a spectral-Galerkin numerical algorithm [J. Shen, *SIAM J. Sci. Comput.*, 15 (1994), pp. 1489–1505]. We impose steady shear to focus on the orientational response of the nanorod ensemble to two experimental controls: the Deborah number ( $De$ ), or normalized imposed shear rate; and physical plate anchoring conditions on the rod ensemble. Our results yield dimensional robustness versus instability of sheared, semidilute, nanorod dispersions: To begin, we present 0-d and 1-d phase diagrams that are consistent with results of the modeling community. Next, we present the first study of numerical stability (for all attractors in the phase diagrams) to 2-d perturbations in the flow-gradient and vorticity directions. The key findings are the following: time-periodic 1-d structure attractors at low-to-moderate  $De$  are robust to 2-d perturbations; period-doubling transitions at intermediate  $De$  to chaotic attractors in 0 and 1 space dimensions are unstable to coherent 2-d morphology but remain chaotic; as  $De$  increases, chaotic dynamics becomes regularized, first to periodic and then to steady structure attractors, along with a return to robust 1-d morphology; finally, logrolling (vorticity-aligned) anchoring selects the most distinct attractors and  $De$  cascade with respect to other anchoring conditions.

**Key words.** nematic polymers, sheared flow, semi-implicit scheme

**AMS subject classifications.** 76A05, 76E30

**DOI.** 10.1137/070707981

**1. Introduction.** Decades of modeling and simulation have been devoted to an understanding of sheared nematic polymers and liquid crystals, motivated by appli-

---

\*Received by the editors November 12, 2007; accepted for publication (in revised form) January 30, 2008; published electronically June 11, 2008. This research was supported in part by the Air Force Office of Scientific Research, Air Force Materials Command, USAF, under grants FA9550-06-1-0063 and FA9550-05-1-0025; by Army Research Office grant ARO 47089-MS-SR; by National Science Foundation DMS awards 0456286, 0610646, 0604891, 0605029, and 0626180; and by NASA-URETI BMat Award NCC-1-02037.

<http://www.siam.org/journals/mms/7-2/70798.html>

<sup>†</sup>Department of Mathematics, University of North Carolina at Chapel Hill, Chapel Hill, NC 27599-3250 (xfyang@email.unc.edu).

<sup>‡</sup>Department of Mathematics and Computer Science, Fayetteville State University, Fayetteville, NC 28314 (zcui@uncfsu.edu).

<sup>§</sup>Department of Mathematics, Institute for Advanced Materials, Nanoscience & Technology, University of North Carolina at Chapel Hill, Chapel Hill, NC 27599-3250 (forest@amath.unc.edu).

<sup>¶</sup>Department of Mathematics, Florida State University, Tallahassee, FL 32306-4510 (wang@math.fsu.edu).

<sup>||</sup>Department of Mathematics, Purdue University, West Lafayette, IN 47907 (shen@math.purdue.edu).

cations to high-performance materials in film and mold geometries, as well as for fundamental interest in the shear-dominated hydrodynamics of anisotropic liquids. Excellent review articles have appeared in the past few years [46, 52, 1]. More emphasis has arisen recently in nematic polymer models and simulation because of their relevance to technological applications of nanocomposites where the nanoparticles are thin rod and platelet inclusions. The physics of these nanorod dispersions surely includes all the basic elements built into liquid crystal polymers and even more complexity such as poor dispersion of the nanoparticle phase. These composites exhibit a diverse range of enhanced properties depending on the specific nanoparticles employed, including mechanical, barrier, dielectric, and conductive properties. However, *three persistent anomalous features in shear-dominated flows have retarded progress in technological applications of nanorod dispersions: particle anisotropy passes up in scale; responses are typically unsteady even in steady driving conditions; and gradient structure develops which translates into heterogeneous materials.* These features are explored and highlighted in the modeling and simulation presented here.

If experiments could be run to observe and probe these anomalies, they would probably not continue to plague film and mold material design and control. The practical reality is that only partial signatures of the rod or platelet distribution functions are measurable, both during and after experiments, and thus the connection between processing controls and material properties is reduced to empirical or ad hoc correlations. This limitation is appreciated with a simple calculation: a typical nanoparticle for material applications is a  $1\text{nm} \times 100\text{nm}$  cylindrical rod, so there are roughly  $10^5$  particles in a cubic micron at 1% volume fraction. One is reduced to measurements that reflect low moments of the particle distribution through scattering intensities. Computational modeling therefore serves as a key for interpreting measurable data and for extrapolating beyond observable features toward design and control strategies for advanced materials. That is the perspective from which we tailor our modeling and simulation approach. From a computational perspective, the above order-of-magnitude calculation makes it apparent that particle simulations are not yet feasible even on cubic millimeter lengthscales and surely not realistic for parameter studies such as those presented here. The Doi–Hess kinetic theory for flowing Brownian rods in the semidilute regime, however, presents a viable alternative; this theory has been the focus of simulations either with the Smoluchowski equation for the orientational probability distribution function or with moment closure models of Landau–de Gennes type.

It is well understood how to coarse-grain the Doi–Hess kinetic model to recover any Landau–de Gennes second-moment tensor model and how to coarse-grain tensor models to recover either the Ericksen or Leslie–Ericksen models [32, 11, 2, 3, 56, 30]. Here “coarse-grain” refers to asymptotic analysis, involving a reduced class of orientational distribution functions (ODFs) (e.g., uniaxial), assumptions on the flow, strength of distortional elasticity, and/or volume fraction of nanoparticles, and closure rules for how to approximate higher moments of the ODF. For the material applications we have in mind, large parameter simulations are required, which are then organized into phase diagrams of response functions. That database then has to be mapped to effective properties. This “processing to property” map has been slow in developing. We give some indications why.

In the simplest, longwave approximation of shear-induced monodomain dynamics (spatially homogeneous or zero-dimensional (0-d), without physical boundary conditions, with a linear shear flow), and in the generalization to 1 dimension (in the shear-gradient direction spanning two parallel plates, with physical anchoring condi-

tions imposed, again with linear flow), phase diagrams are a relatively recent outcome of the modeling community [34, 38, 53, 54, 55, 12, 31, 39, 26, 47, 15, 18, 19, 67]. The slow progress in 0 and 1 dimensions has *not* been due to a computational bottleneck; rather it has been due to the sensitivity of the orientational response to shear-dominated flows, rooted in the three anomalous features discussed next.

First, anisotropy of individual Brownian particles transfers across scales to *anisotropy of the particle orientational distribution*. The orientational distribution of rods or platelets lies somewhere between isotropic (random orientation achieved in equilibrium at sufficiently low volume fractions) and strongly aligned with respect to a single direction (a delta-like distribution, which is approximately achieved in high-speed fiber flows or in small molecule liquid crystals in the presence of magnetic or electric fields). While these are two extremes among all ODFs on the sphere, physical experiments lead somewhere in between. The identification of which nematic polymer ODFs are selected in shear has led to a variety of extensions of liquid crystal theory (which describes a single direction, the major director, under the presumption that the ODF is essentially a delta function) to allow for additional degrees of freedom in the ODF. Ericksen coupled a scalar order parameter to the Leslie–Ericksen director theory in his attempt to bridge director theory with the Landau–de Gennes models based on polymer physics, focusing on the second-moment tensor of the ODF. In the 1970s and 1980s, Hess [27] and Doi [11] developed a Smoluchowski (or Fokker–Planck) equation for the ODF of flowing Brownian rods using the Jeffery orbit for Stokes flow of a rod (prolate spheroid).

The second anomalous feature of sheared rod and platelet dispersions is that the response functions (attractors) are typically *unsteady even in steady processing conditions*. The Jeffery orbit of a single rod in rotational flow is duplicated on the micron scale of tens to hundreds of thousands of nanorods in a dispersion; the ensemble typically exhibits limit cycle responses to shear-dominated flow. Furthermore, nonlocal excluded-volume interactions lead to response functions that are remarkably sensitive to the volume fraction of the rods and shear rate. The tumbling, wagging, and flow-aligning classification of liquid crystals has expanded to the well-documented taxonomy of nematic polymer sheared monodomain response functions: tumbling, wagging, flow-aligning, kayaking and tilted kayaking, steady out-of-plane, logrolling (steady, vorticity aligned), and chaotic. The reader is referred to Larson and Ottinger [34] for the identification of kayaking orbits and to [15] for illustrations and comparisons among all monodomain steady and unsteady response functions.

Here we adopt the following terminology, which has gained traction in the literature. An orientational distribution is called “in-plane” when it is symmetric with respect to the shear plane (the plane of primary flow and flow gradient). In the Cartesian coordinates adopted here,  $x$  is the flow direction,  $y$  is the flow-gradient direction, and  $z$  is then the vorticity axis of an imposed simple shear flow. Thus the second-moment tensor  $\mathbf{M}$  of an in-plane orientational distribution necessarily obeys the constraints  $M_{xz} = M_{yz} = 0$ , which is equivalent to the geometric condition that the vorticity axis  $z$  is an eigenvector. Examples of shear-induced, in-plane monodomain response functions are flow-aligning, a steady state where the principal axis of  $\mathbf{M}$  is uniquely defined and lies in the shear plane; logrolling, a steady state where the principal axis is aligned with the vorticity axis and thus orthogonal to the shear plane; tumbling, a limit cycle response in which the principal axis of  $\mathbf{M}$  rotates continuously in the shear plane; and wagging, a limit cycle response in which the principal axis oscillates in the shear plane with finite amplitude about a given mean angle. Whenever the constraints  $M_{xz} = M_{yz} = 0$  are broken, so that the orthonormal frame of

eigenvectors of  $\mathbf{M}$  does not contain the vorticity axis, the phase is called “out-of-plane.” Examples include out-of-plane steady states, where the principal axis aligns somewhere between the vorticity axis and shear plane; the classical kayaking orbit, where the principal axis (major director) rotates continuously around the vorticity axis; the tilted kayaking orbit, where the principal axis rotates continuously around a direction between the vorticity axis and shear plane; and chaotic orbits, for which the major director migrates erratically around the sphere.

The above two features, anisotropy and unsteady response to steady shear conditions, were studied first in the limit of spatial homogeneity, so-called monodomain models, which solve for orientational response of the rod distribution function to entropic excluded-volume potentials and an imposed linear flow. At the Smoluchowski equation level, the Doi–Hess model is an infinite-dimensional, nonlinear diffusion equation on the sphere; the initial gains in understanding were made at the level of second-moment closure models. Today, a rather complete understanding of the full kinetic model predictions and the approximate nature of second-moment closures is in place. This picture is dominated by numerical results, but analysis has played a critical role in understanding the complexity of kinetic and second-moment tensor monodomain phase diagrams. These predictions are expected to apply in the midgap of parallel-plate shear cells where the flow is approximately linear and the gradients introduced by boundary anchoring have been screened.

Rey and Tsuji were the first to comprehensively address the third persistent feature, *heterogeneity of sheared nematic polymers*, in a multiparameter numerical study. In a seminal paper, Marrucci and Greco [40] introduced a distortional elasticity potential to the Doi–Hess theory, extending the model from homogeneous monodomain dynamics to include heterogeneity. There have been several models of Doi–Marrucci–Greco type which couple to the flow equations; cf. [53, 31, 13, 56]. Rey and Tsuji prudently studied the one-way coupling first, imposing a linear simple shear induced by steady motion of parallel plates, from which they proceeded to numerically map out phase diagrams of one-dimensional (1-d) heterogeneity across the plate gap. Many other leading scientists in the field of nematic liquid crystals and liquid crystal polymers have explored this fundamental question of 1-d morphology and lengthscale selection in shear flow. The imposition of equilibrium anchoring conditions at each plate leads to a spatial conflict between the midgap response function (which is presumably far removed from and free from restrictions imposed by the plates) and the plate equilibrium ODF. Gradients in the ODF ensue, for which distortional elasticity potentials are coupled to the Landau–de Gennes or Doi–Hess model. Outstanding reviews have been written over the years on the issue of sheared heterogeneity, including an especially insightful article by Marrucci and Greco [41] and subsequent excellent reviews by Rey and Denn [46], Tan and Berry [52], and Asokan et al. [1]. (An article of the authors [17] on steady lengthscale selection in the weak shear limit includes a literature discussion which may prove useful.)

The local behavior at each spatial location can be described by one of a variety of monodomain response functions (listed and briefly described above). Thus, heterogeneous attractors are characterized in terms of a small number of layers that span the plate gap, with a fixed monodomain response function per layer. A typical “in-plane heterogeneous attractor” might be “ $\mathbf{W}\text{-}\mathbf{T}$ ,” conveying that layers near each plate consist of local  $\mathbf{W}$  (wagging) limit cycles, whereas in the remaining interior of the gap, the local response is  $\mathbf{T}$  (tumbling). Additional details are associated with each type of heterogeneous 1-d attractor; e.g.,  $\mathbf{W}\text{-}\mathbf{T}$  attractors spawn transient localized defects at the gap heights where the response shifts from finite oscillations

(wagging) to monotone tumbling. We note that no experiment has thus far been able to identify such detail (coexistence of tumbling and wagging), so that measurable signatures that distinguish such attractors need to be identified by modeling. Heterogeneous phase diagrams based on orientation tensor models and imposed shear are given by Tsuji and Rey [54, 55], whereas our group has extended those studies to the Doi–Hess–Smoluchowski equation with resolution in the ODF through tenth moments, including so-called in-plane orientation [20, 21] and full orientational degrees of freedom on the sphere [68, 21]. Our studies, analytical and numerical, predict a strong variability in the heterogeneous response to the plate anchoring conditions, which motivates that focus for this paper as well.

In this hierarchy of models and simulations, there are several directions one can go in relaxing restrictions on orientational and spatial degrees of freedom, each contributing to a comprehensive picture of robustness in physical and orientational space and time. Note that the aforementioned literature begins with homogeneous monodomains in shear, or 0 dimensions, followed by resolution of 1-d spatial gradients along the flow-gradient axis between the two plates and explicit recognition of boundary conditions on orientation. When additional complexity is allowed, an essential question is whether reduced model behavior is persistent or whether the additional degrees of freedom lead one to completely different anisotropy, dynamics, and/or heterogeneity. One important direction is to couple hydrodynamics (and the Navier–Stokes or Stokes equations) to the orientational model, allowing one to explore nonlinear shear profiles generated by orientational stress gradients, and then the feedback from nonlinear shear flow to the ODF. Several major studies of flow-nematic polymer coupling have been undertaken, starting from the Leslie–Ericksen–Frank single director model coupled to flow [4, 5, 53, 54, 55, 14], a “planar” nematic liquid model explored by Kupferman, Kawaguchi, and Denn [31], and full orientation tensor models [53, 54, 55, 16, 13, 49, 22, 8, 28, 29]. All but the last of these studies allow 1-d heterogeneity for fixed orientational boundary conditions.

Our group has explored variability of 1-d heterogeneous responses to plate anchoring conditions, with both orientation tensor [17, 65, 8, 63, 7, 6] and kinetic [68, 20, 65] models, which further reveals sensitivity of flow feedback and morphology to wall anchoring conditions. The Armstrong and Zhang groups [51, 23, 58, 24] have also simulated the kinetic equations with an exploration of the role of translational diffusion, whereas Green, Brown, and Armstrong [24] have further explored different physical models for solid wall boundary conditions. Another direction one can take is to allow for oscillatory plate driving conditions [48, 25, 4, 36, 7, 6] which reveal frequency-dependent storage and loss moduli of nematic polymers.

In this paper, we pursue one pathway of simple-to-complex models, where we successively admit additional orientational degrees of freedom and space dimensions, for variable shear-rate, linear shear flow. We use an orientation tensor model developed by Cui and Wang [9], based on the McMillan continuum mechanical theory for liquid crystals. It is a direct generalization of Leslie–Ericksen (LE) vector theory [35] taking into account biaxiality of the distribution and short-range elasticity through order parameters. We also implement a spectral-Galerkin numerical algorithm [50] that differs from other algorithms, which uses Legendre polynomial bases in the shear gap and Fourier modes in the remaining two space dimensions.

This code allows both the determination of 1-d shear-imposed structure attractors and their robustness to additional spatial degrees of freedom, the focus of the present paper. We perform these dimensional robustness studies for both in-plane orientation tensors, which suppress much of the complex dynamics associated with

kayaking orbits, and full tensors. Even though the in-plane response functions are almost always unstable to out-of-plane orientational modes, they nonetheless are extremely valuable in identifying generic features, such as nontopological defects, in a simple context. The robustness studies are a logical next step in the study of sheared nematic polymers, building on previous seminal foundations: equilibrium phase diagrams from excluded-volume entropic interactions, which date back to Onsager [44] and explain experimental hysteresis in isotropic and nematic phases; bulk monodomain phase diagrams versus imposed steady shear rate (the Deborah number when normalized by the orientational relaxation rate), which explain steady and unsteady experimental responses and new dynamical phenomena such as tumbling, wagging, kayaking, and chaotic dynamics in steady shear; and 1-d confinement-induced spatial heterogeneity, which arises when one accounts for physical orientational boundary conditions at solid walls. The significant investments in building these foundations provide insight for each subsequent level of description of sheared nematic polymer complexity.

The remaining steps *beyond the present paper* include flow coupling and model efficacy with respect to experiments. Leal and coworkers [28, 29] have developed and simulated two-dimensional (2-d) algorithms for their second-moment tensor models, focusing thus far on roll cells [33] at low  $De$  and their breakup processes, restricted to vorticity-aligned plate anchoring boundary conditions. Since we impose simple shear hydrodynamics for this paper, we can make contact with their work only by comparing our 2-d orientational morphologies with vorticity-aligned anchoring, which we comment on in the concluding remarks.

Before launching into results of our simulations, we summarize the strategy that dictates the order of our presentation. The longwave, monodomain limit predicts the free-space (0-d) response (independent of physical boundary conditions on the orientational distribution) to an imposed linear shear flow. The response diagram of interest consists of solution curves versus normalized shear rate ( $De$ ), of all steady and unsteady response functions, recalled from [15]. This corresponds to the infinite  $Er$  limit of the full PDE model, which decouples spatial structure and the physical boundary conditions at the plates. As we shall illustrate, the monodomain responses for each  $De$  allow one to predict, and guide the interpretation of, morphology attractors. In the interior of a plate gap, anchoring is screened, and the monodomain response is natural unless other physics overwhelms the free-space response (e.g., a sufficiently strong distortional elasticity potential will arrest tumbling). Next, we admit 1-d spatial heterogeneity and explicitly account for the physical plate anchoring on orientation. We present results of a comprehensive numerical study through 1-d attractor phase diagrams, versus  $De$  as in the monodomain diagram, and for a sample of five different anchoring conditions. We fix the strength of the distortional elasticity potential, parametrized by the Ericksen number  $Er$ , so that the nematic liquid does not arrest all dynamical responses.

These 1-d phase diagrams benchmark the model and code against the previous 1-d tensor and kinetic model predictions cited earlier. Results are presented both for restricted in-plane orientation tensors and for full orientational degrees of freedom; we thus determine the coexistence of 1-d heterogeneous attractors, where the in-plane attractors are typically unstable to out-of-plane perturbations. Finally, the algorithm is implemented to explore the robustness and stability of all attractors in these 1-d phase diagrams to 2-d noisy perturbations in the vorticity ( $z$ ) direction as well as flow-gradient ( $y$ ) direction.

We are motivated by 2-d results of Leal's group [28, 29], but also by the funda-

mental issue of whether anchoring conditions and  $De$  variations select stable 1-d or full 2-d responses. We call attention to sensitivities to wall orientational anchoring conditions, reported experimentally by the Noirez lab [45, 42, 43] and exhibited in our modeling [17, 7, 8, 65]. These studies guide our presentation of the  $De$  cascade in 1 and 2 dimensions for a discrete set of anchoring conditions, including logrolling as in [29], tangential and normal anchoring with respect to the plates, and a tilted anchoring condition midway between the vorticity axis and shear plane. We believe these studies provide insight into more complex flows, such as in mold filling, where there is no way to uniformly control anchoring relative to flow geometry; as we will see, anchoring conditions can have a dramatic impact. While we consider spatial perturbations in the flow-gradient and vorticity directions here, a similar study of 2-d perturbations including the flow direction is deferred to another study, as well as the significant challenges of phase diagrams in 3 dimensions and with full flow coupling. The Leal group has reported full three-dimensional (3-d) simulations with full coupling in recent conference lectures (presented by Carlos Garcia-Cervera) and in an article recently accepted for publication in the *Journal of Rheology*; again they explore logrolling boundary conditions.

We foreshadow the intriguing observation from results presented below: with an imposed simple linear shear flow with varying shear rate, we recover the diversity of 1-d orientational responses that have been reported with full flow coupling and nonlinear feedback. The generality of this observation to higher space dimensions remains to be explored, but, where valid, it would represent a significant computational cost savings in that the Navier–Stokes solver could be decoupled for large parameter studies and implemented only as a corrector step (using the paradigm promoted by Yannis Kevrekidis in the past few years) in parameter regimes of interest where quantitative details are important.

## 2. The model and numerical method.

**A. Model formulation.** To describe the local ordering of nematic (liquid crystal) polymers, we employ a second-order, symmetric, traceless tensor  $\mathbf{Q}$ , which is often called the orientation tensor of Landau–de Gennes theory. The orientation tensor is the traceless normalization of the second moment  $\mathbf{M}$  of the orientational probability distribution function, i.e.,  $\mathbf{Q} = \mathbf{M} - \frac{1}{3}\mathbf{I}$ , so that these two rank 2 tensors share an orthonormal frame of principal axes, called the directors in the nematic liquid literature. The Cartesian representation employed here is given relative to an imposed simple shear flow,

$$(1) \quad \mathbf{v} = (v_x, v_y, v_z) = \dot{\gamma}(y, 0, 0),$$

where  $x$  is the primary flow direction,  $y$  is the flow-gradient axis between the two parallel plates, and  $z$  is the vorticity axis. The representation of  $\mathbf{Q}$ , since  $\text{tr}(\mathbf{Q}) = 0$ , is then

$$(2) \quad \mathbf{Q} = \begin{pmatrix} Q_{xx} & Q_{xy} & Q_{xz} \\ Q_{xy} & Q_{yy} & Q_{yz} \\ Q_{xz} & Q_{yz} & -Q_{xx} - Q_{yy} \end{pmatrix}.$$

We employ a mesoscopic tensor model [9] based on a tensor-based hydrodynamic theory for flows of nematic liquid crystal polymers [37]. This model is of Landau–de Gennes type [10] and therefore similar to all second-moment tensor models used in nematic polymer morphology studies [53, 54, 55, 49, 31, 15, 63, 64]:

$$\begin{aligned}
 (3) \quad & \frac{\partial \mathbf{Q}}{\partial t} + \mathbf{v} \cdot \nabla \mathbf{Q} - \Omega \cdot \mathbf{Q} + \mathbf{Q} \cdot \Omega - a[\mathbf{D} \cdot \mathbf{Q} + \mathbf{Q} \cdot \mathbf{D}] = -\frac{2a}{3}\mathbf{D} - 2a(\mathbf{Q} : \mathbf{D})(\mathbf{Q} + \frac{\mathbf{I}}{3}) \\
 & - \frac{\nu k T}{\alpha} [\frac{3}{2}(1 - \frac{N}{3})\mathbf{Q} - \frac{3}{2}N(\mathbf{Q}^2 - \frac{1}{3}(\mathbf{Q} : \mathbf{Q})\mathbf{I}) + 3N(\mathbf{Q}^3 - \frac{1}{3}\text{tr}(\mathbf{Q}^3))] \\
 & + L_1 \Delta \mathbf{Q} + \frac{L_2}{2}[\nabla \nabla \cdot \mathbf{Q} + (\nabla \nabla \cdot \mathbf{Q})^T - \frac{2}{3}\text{tr}(\nabla \nabla \cdot \mathbf{Q})\mathbf{I}] \\
 & + \frac{L_3}{2}[\nabla \mathbf{Q} : \nabla \mathbf{Q} - \frac{1}{3}\text{tr}(\nabla \mathbf{Q} : \nabla \mathbf{Q})\mathbf{I} + 2(\nabla \cdot \mathbf{Q}) \cdot \nabla \mathbf{Q} + 2\mathbf{Q} : \nabla \nabla \mathbf{Q}],
 \end{aligned}$$

where  $\hat{\mathbf{Q}} = \dot{\mathbf{Q}} + \mathbf{Q} \cdot \Omega - \Omega \cdot \mathbf{Q}$  is the upper convected derivative,  $\mathbf{D} = \frac{1}{2}(\nabla \mathbf{v} + (\nabla \mathbf{v})^t)$  is the rate-of-strain tensor, and  $\Omega = \frac{1}{2}(\nabla \mathbf{v} - (\nabla \mathbf{v})^t)$  is the vorticity tensor,  $a$  is a geometric parameter, with  $0 < a \leq 1$  for rods and  $-1 \leq a < 0$  for platelets,  $\nu$  is the nematic polymer density,  $k$  is the Boltzmann constant,  $T$  is absolute temperature,  $\alpha$  is a viscosity parameter, and  $L_1, L_2, L_3$  are the distortional elasticity constants. For uniaxial orientational distributions, where  $\mathbf{Q} = s(\mathbf{n}(\mathbf{x}, t)\mathbf{n}(\mathbf{x}, t) - \frac{\mathbf{I}}{3})$ , there is a single nonzero order parameter ( $s$ ) and a unique major director ( $\mathbf{n}$ ); in the weak flow limit, the elasticity constants can be identified with the three Frank elastic constants of liquid crystal theory, splay ( $K_1$ ), twist ( $K_2$ ), and bend ( $K_3$ ):

$$(4) \quad L_1 = \frac{3K_2 - K_1 + K_3}{6s^2}, \quad L_2 = \frac{K_1 - K_2}{s^2}, \quad L_3 = \frac{K_3 - K_1}{2s^3}.$$

The precise value of  $s$  is the equilibrium value of (3) in the absence of flow ( $\mathbf{v} = 0$ ), set by the normalized rod volume fraction  $N$ .

Thermodynamic stability requires that

$$(5) \quad K_1 \geq 0, \quad K_2 \geq 0, \quad K_3 \geq 0.$$

These inequalities lead to

$$(6) \quad \begin{aligned}
 L_1 &\geq 0, & 2L_1 + L_2 &\geq 0, \\
 -\frac{3}{2}(L_1 + \frac{1}{2}L_2) &\leq L_3 s \leq 3(L_1 + \frac{1}{2}L_2).
 \end{aligned}$$

In addition, for rodlike particles [2, 56, 57, 30],

$$(7) \quad K_2 < K_1 < K_3,$$

which translates into

$$(8) \quad L_2 \geq 0, \quad L_3 \geq 0,$$

whereas for platelets,

$$(9) \quad K_3 < K_1 < K_2,$$

leading to

$$(10) \quad L_2 \leq 0, \quad L_3 \leq 0.$$

The computational domain is a 1-d interval  $[-h, h]$  or a 2-d box of dimensions  $[-h, h] \times [0, 2\pi h]$ . Scaling by the half gap width  $h$  and the relaxation time scale  $t_0 = \frac{\alpha}{\nu k T}$ , we define dimensionless variables as

$$(11) \quad \tilde{\mathbf{x}} = \frac{\mathbf{x}}{h}, \quad \tilde{t} = \frac{t}{t_0}, \quad \tilde{\mathbf{v}} = \frac{h}{t_0} \mathbf{v}.$$

The following dimensionless parameters arise in the model equations:

$$(12) \quad Er = \frac{h^2}{L_1}, \quad De = \dot{\gamma} t_0, \quad \theta_2 = \frac{L_2}{L_1}, \quad \theta_3 = \frac{L_3}{L_1}.$$

The dimensionless flow field becomes

$$(13) \quad \mathbf{v} = De(y, 0, 0),$$

where  $De$  is the *Deborah* number, the dimensionless shear rate, and  $Er$  is the Ericksen number (normalized strength of the distortional elasticity potential). It is worthy to note that the various models in the literature lead to different definitions of the fundamental dimensionless parameters, mainly due to the starting point (irreversible thermodynamics, continuum mechanics, or molecular kinetic theory). Of particular note, many authors incorporate the flow into the definition of the Ericksen number, which can easily be done by defining a new Ericksen number as the product of  $Er$  above with  $De$ . We depart from this convention, decoupling the flow from the Ericksen number, so that the infinite Ericksen number limit yields the monodomain model for simple shear where the distortional elasticity potential is eliminated. Our convention is also employed by Rey's group, whereas the Leal, Denn, and Hess groups have linked the Ericksen number to flow. Nonetheless, the mathematical form of the model equations at the scale of the second-moment tensor is quite robust, so that one can draw tight analogies between the Deborah and Ericksen numbers among the various models.

We will drop the tilde overbar  $\tilde{\cdot}$  in the remainder of this paper, with all graphs in nondimensional variables. The dimensionless form of (3) is

$$(14) \quad \begin{aligned} & \frac{\partial \mathbf{Q}}{\partial t} + \mathbf{v} \cdot \nabla \mathbf{Q} - \Omega \cdot \mathbf{Q} + \mathbf{Q} \cdot \Omega - a[\mathbf{D} \cdot \mathbf{Q} + \mathbf{Q} \cdot \mathbf{D}] = -\frac{2a}{3} \mathbf{D} - 2a \mathbf{D} : \mathbf{Q} (\mathbf{Q} + \frac{1}{3} \mathbf{I}) \\ & - [\frac{3}{2}(1 - \frac{N}{3}) \mathbf{Q} - \frac{3}{2} N (\mathbf{Q}^2 - \frac{1}{3} (\mathbf{Q} : \mathbf{Q}) \mathbf{I}) + 3N (\mathbf{Q}^3 - \frac{1}{3} \text{tr}(\mathbf{Q}^3))] + \frac{1}{Er} \Delta \mathbf{Q} \\ & + \frac{\theta_2}{2Er} [\nabla \nabla \cdot \mathbf{Q} + (\nabla \nabla \cdot \mathbf{Q})^T - \frac{2}{3} \text{tr}(\nabla \nabla \cdot \mathbf{Q}) \mathbf{I}] \\ & + \frac{\theta_3}{2Er} [\nabla \mathbf{Q} : \nabla \mathbf{Q} - \frac{1}{3} \text{tr}(\nabla \mathbf{Q} : \nabla \mathbf{Q}) \mathbf{I} + 2(\nabla \cdot \mathbf{Q}) \cdot \nabla \mathbf{Q} + 2\mathbf{Q} : \nabla \nabla \mathbf{Q}], \end{aligned}$$

and (6) leads to

$$(15) \quad \theta_2 \geq -2, \quad -\frac{3}{2}(1 + \frac{1}{2}\theta_2) \leq \theta_3 s \leq 3(1 + \frac{1}{2}\theta_2).$$

In this paper, we will focus on the case of rod-like macromolecules with equal splay and bend constants, i.e.,  $\theta_3 = 0$ . The dimensionless computational domain in physical space  $(x, y, z)$  is  $[0, 2\pi] \times [-1, 1] \times [0, 2\pi]$ , which allows physical plate anchoring conditions on the plates  $(y = -1, 1)$  and periodic conditions otherwise.

It is useful to write  $\mathbf{Q}$  in the following spectral form:

$$(16) \quad \mathbf{Q} = s(\mathbf{n}_1 \mathbf{n}_1 - \frac{1}{3} \mathbf{I}) + \beta(\mathbf{n}_2 \mathbf{n}_2 - \frac{1}{3} \mathbf{I}),$$

where  $s = d_1 - d_3$  and  $\beta = d_2 - d_3$ , and  $d_1, d_2$ , and  $d_3$  are the eigenvalues of  $\mathbf{M} = \mathbf{Q} + \frac{1}{3} \mathbf{I}$  satisfying  $0 \leq d_3 \leq d_2 \leq d_1 \leq 1$  and  $d_1 + d_2 + d_3 = 1$ .

The *order parameters*  $s$  and  $\beta$  obey  $s \geq \beta \geq 0$ , where the equalities define special configurations; when  $s > 0$ ,  $\mathbf{n}_1$  is uniquely defined and is called the major director; when  $s \geq 0$  and  $\beta = 0$ , the orientation is uniaxial, whereas  $s > 0$  and  $\beta > 0$  correspond to biaxial phases. Orientational degeneracies arise when  $s = 0$  (the isotropic phase) or  $s = \beta \neq 0$ , which corresponds to order-parameter defects in which the major axis of orientation is not unique but rather lies on a circle. This type of defect is often called an oblate phase, since the triaxial ellipsoid defined by the positive-definite second-moment tensor  $\mathbf{M} = \mathbf{Q} + \frac{1}{3} \mathbf{I}$  is an oblate spheroid, where the principal axes obey  $d_1 = d_2 > d_3$ . In nondefect phases, the triaxial ellipsoid defined by  $\mathbf{M}$  is a prolate

spheroid in the nematic equilibrium phase (where  $d_1 > d_2 = d_3$ , or  $s > 0, \beta = 0$ ) and a triaxial ellipsoid otherwise (with  $d_1 > d_2 > d_3 > 0$ , or  $s > 0, \beta > 0$ ). In the figures below, we will illustrate these nontopological defects by snapshots of the spatial distribution of  $\mathbf{M}$  tensor orientational ellipsoids. The power of these figures is that, in addition to nontopological defects which are independent of space dimensions, the more traditional topological defects—defined by winding number invariants around a closed curve in 2 or 3 space dimensions of a presumed uniquely defined major director axis—are also easily identified in 2-d morphologies.

It is traditional to illustrate, classify, and quantify orientational distributions in terms of the spectral representation of  $\mathbf{Q}$  (equivalently,  $\mathbf{M}$ ), with figures of scalar order parameters ( $s$  and  $\beta$ ) and the major director  $\mathbf{n}_1$ . We caution that a focus on  $\mathbf{n}_1$  is potentially misleading. A precipitous drop in  $s = d_1 - d_3$  or  $s - \beta = d_1 - d_2$  corresponds to a defocusing of the orientational distribution and passage to either an oblate defect phase ( $s - \beta = 0, s > 0$ ) or an isotropic phase ( $s = 0$ , so that all  $d_i = \frac{1}{3}$ ). In the oblate defect phase, the “major director” lies on the circle spanned by the principal axes of the double eigenvalue  $d_1$ , and, in the isotropic phase, the major director is anywhere on the sphere. It will be shown that oblate defect phases are quite common in sheared nematic polymer layers, yet isotropic defects are not observed. Thus, it is necessary to monitor the order parameters when looking at “director distributions” to fully appreciate the focusing and defocusing of the rod ensemble. Rather than look at these eigenvalue and eigenvector features separately, we present graphics of the full  $\mathbf{M}$  tensor ellipsoids across the gap and in time, which combines all the information contained in the directors and the order parameters. Nonetheless, we also follow tradition with graphs of the major director  $\mathbf{n}_1$ , in particular the “in-plane” angle  $\phi$ , measured counterclockwise from the positive  $x$ -axis, and “out-of-plane” angle  $\psi$ , measured from the shear ( $x$ - $y$ ) plane toward the positive  $z$ -axis:

$$(17) \quad \mathbf{n}_1 = (\cos \psi \cos \phi, \cos \psi \sin \phi, \sin \psi).$$

Note in the figures to follow that  $\psi = 0$  corresponds to in-plane orientation where  $\mathbf{n}_1$  lies in the shear ( $x$ - $y$ ) plane, while  $\psi = \frac{\pi}{2}$  corresponds to vorticity alignment of  $\mathbf{n}_1$ , also known as logrolling alignment. The graphs of  $\psi$  and  $\phi$  therefore quickly identify distinctions between various local orientational phases. For example, the kayaking limit cycle corresponds to an oscillation of  $\psi$  about  $\psi = \frac{\pi}{2}$ , while the in-plane angle  $\phi$  continuously rotates; the tilted kayaking limit cycle consists of an oscillation of  $\psi$  about an axis between 0 and  $\pi/2$ , and the in-plane angle  $\phi$  also oscillates with finite amplitude.

**B. Computational methods and boundary data.** The model (14) consists of a system of nonlinear parabolic PDEs for  $\mathbf{Q}$ , with the following generic structure:

$$(18) \quad \frac{\partial \mathbf{Q}}{\partial t} - \frac{1}{Er} \Delta \mathbf{Q} = \mathbf{F}(\mathbf{Q}).$$

We use a standard backward difference scheme for time discretization and second-order extrapolation for the nonlinear functional  $F(\mathbf{Q})$ . The second-order semi-implicit scheme in time is then

$$(19) \quad \frac{3\mathbf{Q}^{n+1} - 4\mathbf{Q}^n + \mathbf{Q}^{n-1}}{2\delta t} - \frac{1}{Er} \Delta \mathbf{Q}^{n+1} = 2\mathbf{F}(\mathbf{Q}^n) - \mathbf{F}(\mathbf{Q}^{n-1}),$$

where  $Q^n = Q(t = t_n)$  and  $\delta t$  is the time step. We illustrate the method in 3-d space  $(x, y, z) \in [-1, 1] \times [0, 2\pi] \times [0, 2\pi]$ . In the 1-d case, we seek numerical solutions that

are homogeneous in  $(y, z)$ , whereas we seek solutions that are homogeneous in  $z$  in the 2-d case. For spatial discretization, we use the fast Fourier transform in  $z$  and  $x$  and a Legendre polynomial basis in  $y$ . In particular, let  $Q(x, y, z)$  denote any component of  $\mathbf{Q}$ :

$$(20) \quad Q(x, y, z) = \tilde{Q}(y) + \sum_{n=-N/2}^{N/2} \sum_{k=0}^{K-2} \sum_{m=-M/2}^{M/2} a_{n,k,m} e^{inx} \psi_k(y) e^{imz},$$

where

$$(21) \quad \tilde{Q}(y) = \frac{Q(x, 1, z) - Q(x, -1, z)}{2} y + \frac{Q(x, 1, z) + Q(x, -1, z)}{2},$$

$$(22) \quad \psi_k(y) = L_k(y) - L_{k+2}(y).$$

In the above,  $L_k$  is the  $k$ th-order Legendre polynomial;  $\tilde{Q}(y)$  satisfies the nonhomogeneous boundary condition at  $y = \pm 1$ . In 1-d simulations,  $Q(y) = \sum_{k=0}^{K-2} a_k \psi_k(y) + \tilde{Q}(y)$ . In 2-d simulations in  $(y, z)$ ,

$$(23) \quad Q(y, z) = \sum_{k=0}^{K-2} \sum_{m=-M/2}^{M/2} a_{k,m} \psi_k(y) e^{imz} + \tilde{Q}(y).$$

In the graphs below we will show the dynamics of a randomly chosen 2-d amplitude function  $a_{k,m}$  after it has been populated with small noise, in order to explore the stability of 1-d attractors. Further details of the numerical method can be found in [50] and subsequent papers. In the numerical simulations we presented here, for all 1-d simulations with  $y \in [-1, 1]$ , we use the 128 Legendre modes. For all 2-d simulations with  $(y, z) \in [-1, 1] \times [0, 2\pi]$ , we use 128 Legendre polynomials and 128 Fourier modes.

*Boundary conditions on the orientational distribution.* We assume that  $\mathbf{Q}$  is in static equilibrium at the plates, which means  $\mathbf{Q}$  is uniaxial ( $s \neq 0, \beta = 0$ ) at  $y = \pm 1$ , with  $s_0$  prescribed by the normalized volume fraction  $N$ ,

$$(24) \quad s_0 = \frac{1}{4} \left( 1 + 3\sqrt{1 - \frac{8}{3N}} \right),$$

while the major director  $\mathbf{n}_0$  is arbitrary. Thus, one has the ability to prescribe any principal axis of orientation at the plates. This leads to the parameterized boundary conditions on  $\mathbf{Q}$ :

$$(25) \quad \mathbf{Q}(y = \pm 1) = s_0(\mathbf{n}_0 \mathbf{n}_0 - \frac{\mathbf{I}}{3}).$$

In the studies to follow, we consider the following five choices of anchoring conditions on  $\mathbf{n}_0$ , which are in order of presentation, parallel to the plates and along the flow direction, homeotropic or orthogonal to the plates, tilted in-plane midway between the flow and flow-gradient axes, tilted out-of-plane, and logrolling (along the vorticity axis, perpendicular to the shear plane):

$$(26) \quad \mathbf{n}_0 = \begin{pmatrix} 1 \\ 0 \\ 0 \end{pmatrix}, \quad \begin{pmatrix} 0 \\ 1 \\ 0 \end{pmatrix}, \quad \begin{pmatrix} \frac{1}{\sqrt{2}} \\ \frac{1}{\sqrt{2}} \\ 0 \end{pmatrix}, \quad \begin{pmatrix} \frac{1}{\sqrt{3}} \\ \frac{1}{\sqrt{3}} \\ \frac{1}{\sqrt{3}} \end{pmatrix}, \quad \begin{pmatrix} 0 \\ 0 \\ 1 \end{pmatrix}.$$

In the flow ( $x$ ) and vorticity ( $z$ ) directions, we assume that  $\mathbf{Q}$  satisfies periodic boundary conditions. For this paper, we will suppress variations in the flow direction.

It is worth mentioning that simulations with “in-plane orientation” will always yield in-plane response functions when the constraints  $Q_{xz} = 0$  and  $Q_{yz} = 0$  are obeyed at the walls and in the initial data. The in-plane invariant subspace has been exploited in many studies in the past to simplify the dynamics, to analytically explore effects of orientational confinement, or to identify responses which are stable within this confined space of orientations. For in-plane attractors, we impose these constraints; for out-of-plane attractors, we initialize  $Q_{xz}$  and  $Q_{yz}$ , with infinitesimal white noise with  $O(10^{-4})$  amplitude, and report whether the evolution is back to in-plane confined attractors or to full tensor structures. A simple comparison of the in-plane attractor (Table 1) and out-of-plane attractor (Table 2) conveys that most (but not all) in-plane attractors are unstable to out-of-plane tensor degrees of freedom, independent of the number of space dimensions (0, 1, or 2). Similarly, we report results of dimensional stability within in-plane symmetry constraints, where the 2-d modal amplitudes  $a_{k,m}$  of the Fourier–Legendre basis in  $y, z$  are populated with weak noise on top of any snapshot of a 1-d attractor.

Throughout this paper, we fix the particle geometry parameter  $a = 0.8$  and the normalized volume fraction  $N = 6$ ; these values are consistent with our earlier studies of monodomain and 1-d structure attractors [15, 8, 6], which give the best accuracy with full orientational distribution function resolution from Doi–Hess kinetic model simulations [19]. We further fix the Ericksen number at  $Er = 1000$ , which is sufficiently high, so that we access complex dynamic and spatial morphologies. We have performed simulations at a variety of  $Er$ , but the results presented are the most informative relative to the previous literature.

**3. Structure attractors: 0, 1, and 2 space dimensions.** We begin with the 0-d monodomain bifurcation diagram (attractors versus  $De$ ), Figure 1, followed by phase diagrams of in-plane (Table 1) and out-of-plane (Table 2) 1-d structure attractors versus  $De$  for five wall anchoring conditions, and then stability to 2-d perturbations for the full phase diagrams. Each attractor is determined by long-time simulations so that transients have passed. This section is devoted to the details of individual attracting states and how the hierarchy of attractors relates to one another. As discussed above, these attractor diagrams successively admit additional orientational or spatial degrees of freedom, so that each successive diagram conveys robustness or instability of the previous reduced-order model as configuration or physical space constraints are released.

Figure 1 depicts homogeneous monodomain response functions versus  $De$ , summarized from [15], which apply since the infinite  $Er$  limit of our model reduces to the so-called Doi closure model for monodomain dynamics. These diagrams give the “free space” attractors both for in-plane and full orientational degrees of freedom, where the effects of physical plate anchoring are suppressed. We often illustrate a structure attractor in terms of the monodomain response at fixed spatial locations. As we shall illustrate, these longwave results are excellent predictors of behavior locally in the center of the shear gap, including fixed  $De$  responses and their transitions (bifurcations). We simply note that this correlation of monodomain  $De$  cascades with 1-d heterogeneous cascades implies that the structure cascades possess longwave instabilities.

Table 1 presents the 1-d attractor type for in-plane orientation tensors and heterogeneity in 1 space dimension ( $y$ ). Additionally, dimensional robustness or instability

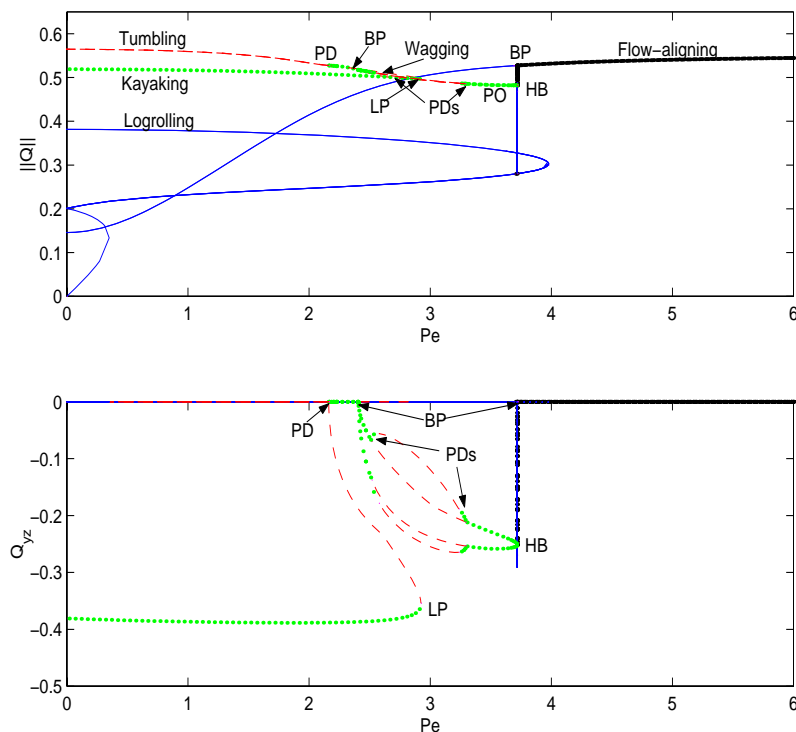


FIG. 1. The monodomain bifurcation diagram from [15] for normalized shear rates  $0 \leq Pe \leq 6$ , where  $De$  of this paper is proportional to  $Pe$ .  $\|\mathbf{Q}\|$  denotes the 2-norm for the second-order tensor  $\mathbf{Q}$ . All transitions (bifurcations) occur within the normalized shear rates  $0 \leq Pe \leq 6$ , beyond which the unique attractor is an in-plane flow-aligned state. Black (dark solid) and green (dotted) branches are stable; blue (solid) and red (dashed) branches are unstable. The bottom graph is the out-of-plane component  $Q_{yz}$ , whose nonzero values distinguish out-of-plane solutions. Between the two pitchfork bifurcations  $BP$  that mark in-plane to out-of-plane transitions at  $Pe \approx 2.4$  and  $3.7$ , we give both the maximum and minimum values of  $Q_{yz}$ . The bifurcation labels are  $PD$  for period-doubling,  $HB$  for Hopf,  $BP$  for pitchfork, and  $LP$  for a saddle-node bifurcation of out-of-plane periodic states. A cascade of  $PD$  bifurcations leading into and out of a window of chaotic attractors for  $2.92 < Pe < 3.25$  is resolved. Reprinted with kind permission from Springer Science + Business Media: *Rheologica Acta*, Monodomain response of finite-aspect-ratio macromolecules in shear and related linear flows, Volume 42, 2003, pages 20–46, M. Gregory Forest and Qi Wang, Figure 8.

TABLE 1

1-d phase diagram and dimensional stability for confined in-plane orientation tensors with the symmetry constraints  $Q_{xz} = Q_{yz} = 0$  imposed versus Deborah number  $De$  and plate anchoring boundary condition on the major director  $\mathbf{n}_0$ . Each entry contains the 1-d heterogeneous attractor type and either “–1” if the solution is stable to 2-d perturbations or “–2” if the solution is unstable to 2-d perturbations with convergence to full 2-d structure.

$\mathbf{n}_0 \setminus De$	2	3.5	3.75	4	4.5	4.75	5	5.5	6
(1, 0, 0)	W-T –1	W –2	W –2	W –2	FA –2	FA –2	FA –2	FA –1	FA –1
(0, 1, 0)	W-T –1	W –2	W –2	W –2	FA –2	FA –2	FA –2	FA –1	FA –1
(0, 0, 1)	LR –1	LR –2	LR-FA –1						

is conveyed: the 1-d attractor is stable to noisy 2-d perturbations if –1 appears after the attractor type, or unstable if –2 appears, indicating growth of the perturbations and saturation to a full 2-d spatial morphology. For this paper, we consider periodic boundary conditions in the vorticity direction  $z$ , as in [28, 29].

TABLE 2

1-d phase diagram and dimensional stability for full orientational degrees of freedom versus Deborah number  $De$  and plate anchoring boundary condition on the major director  $\mathbf{n}_0$ . Each table entry conveys the 1-d heterogeneous attractor type, followed by “-1” if that solution is stable to 2-d perturbations and by “-2” if the solution is unstable to 2-d perturbations, leading to full 2-d morphology.

$\mathbf{n}_0 \setminus De$	2	3.5	3.75	4	4.5
(1, 0, 0)	$\mathbf{K}_2\mathbf{K}_1 - 1$	$\mathbf{K}_2 - 2$	$\mathbf{K}_2\mathbf{K}_1 - 2$	$\mathbf{CH} - 2$	$\mathbf{CH} - 2$
(0, 1, 0)	$\mathbf{K}_2\mathbf{K}_1 - 1$	$\mathbf{K}_2 - 1$	$\mathbf{K}_2\mathbf{K}_1 - 2$	$\mathbf{CH} - 2$	$\mathbf{CH} - 2$
(1, 1, 1)	$\mathbf{K}_2\mathbf{K}_1 - 1$	$\mathbf{K}_2\mathbf{K}_1 - 1$	$\mathbf{K}_2\mathbf{K}_1 - 1$	$\mathbf{CH} - 2$	$\mathbf{CH} - 2$
(0, 0, 1)	$\mathbf{K}_1 - 1$	$\mathbf{K}_1 - 1$	$\mathbf{K}_1 - 1$	$\mathbf{K}_1 - 1$	$\mathbf{K}_1 - 2$

$\mathbf{n}_0 \setminus De$	4.75	5	5.5	5.625	6
(1, 0, 0)	$\mathbf{CH} - 2$	$\mathbf{CH} - 2$	$\mathbf{K}_2 - 1$	$\mathbf{FA} - 1$	$\mathbf{FA} - 1$
(0, 1, 0)	$\mathbf{CH} - 2$	$\mathbf{K}_2 - 2$	$\mathbf{K}_2 - 1$	$\mathbf{FA} - 1$	$\mathbf{FA} - 1$
(1, 1, 1)	$\mathbf{CH} - 2$	$\mathbf{K}_2 - 1$	$\mathbf{K}_2 - 1$	$\mathbf{OS} - 1$	$\mathbf{OS-FA} - 1$
(0, 0, 1)	$\mathbf{CH} - 2$	$\mathbf{CH} - 2$	$\mathbf{CH} - 2$	$\mathbf{K}_2 - 1$	$\mathbf{OS-FA} - 1$

Table 2 presents the same information as Table 1, except with full orientational degrees of freedom. These diagrams give attractors versus two experimental controls: the Deborah number  $De$ , which parametrizes the bulk imposed shear rate relative to the nematic polymer relaxation time and is controlled by plate speed and plate separation distance; and the wall anchoring boundary condition that selects the primary orientation axis  $\mathbf{n}_0$  at each plate, which is typically controlled by mechanical or chemical treatment.

**3.1. Table 1: In-plane 1-d heterogeneous attractors and their stability to 2-d perturbations.** When plate anchoring boundary conditions lie in the shear plane (of the primary flow ( $x$ ) and flow-gradient ( $y$ ) directions), there is a strong bias toward orientational distributions where the out-of-plane components are negligible:  $Q_{xz} = Q_{yz} = 0$ . Often these in-plane response functions are unstable to out-of-plane perturbations, yet they are valuable nonetheless in explaining fundamental behavior. Thus, it is prudent to explore in-plane orientational responses and then their stability to out-of-plane degrees of freedom. This subject has attracted significant attention in the literature, especially since the model equations are far more tractable and even explicitly solvable in many situations. Sometimes the instabilities to out-of-plane modes are extremely weak and may take hundreds if not thousands of relaxation times to emerge [62]. The monodomain diagram, Figure 1 from [15], yields that in the nematic concentration range of this paper, the low  $De$  in-plane response is “tumbling” (continuous rotation of the major axis of orientation), which gives way to “wagging” (finite oscillations) and finally steady flow alignment as  $De$  increases. These longwave responses will emerge as accurate predictors of midgap behavior in heterogeneous simulations.

The outlier in this picture surrounds the logrolling steady state with in-plane constraints. There is no freedom for the major director (peak orientation axis) to pass from vorticity alignment to any other direction: the  $Q_{xz} = Q_{yz} = 0$  constraints allow either vorticity alignment or any direction orthogonal (i.e., in the shear plane). The only pathway is therefore through an order-parameter degeneracy, or defect phase. From Table 1, when logrolling boundary conditions are imposed together with in-plane symmetry for sufficiently small  $De$ , the response is steady with logrolling orientation throughout the shear gap; note this is in stark contrast with any other low  $De$  response. The other available monodomain in-plane responses, namely tumbling or

wagging, are simply in conflict with the symmetry and boundary constraints. A composite heterogeneous response that is vorticity-aligned at the plates and tumbling in the interior would require a discontinuity at the boundary. As  $De$  increases, however, the stable monodomain response switches to in-plane flow alignment, which is compatible with the logrolling boundary condition *only* through a defect phase somewhere in the gap! Namely, the order parameters must allow either for a 2-d eigenspace of the largest eigenvalue,  $d_1 = d_2 \neq d_3$ , or for an isotropic phase where all  $d_i = \frac{1}{3}$ . The former case turns out to be preferred, leading to a steady structure with an oblate defect phase. This is effectively visualized in terms of the second-moment ( $\mathbf{M}$ ) tensor ellipsoid, as described earlier. Confined in-plane attractors are therefore especially useful for gaining insight into shear-induced nontopological defects, due to order parameter degeneracies. These defects are not limited to in-plane symmetry, but they are easily prescribed and explained with in-plane confined symmetry. Nontopological defects are totally absent in liquid crystal director theories, which possess only director or topological defects, which are furthermore possible only in 2 dimensions or greater. This is one of the most striking differences between director and tensor or kinetic models: nontopological defects can arise even in monodomains (0 dimensions) or in 1 dimension.

Now, with coupled physical boundary conditions at the plates and distortional elasticity, we simulate three different anchoring conditions (tangential, normal, and vorticity-alignment (logrolling)), each respecting the in-plane symmetries  $Q_{xz} = Q_{yz} = 0$ . Five different structure attractors arise, which we label according to the nomenclature first introduced by Tsuji and Rey [53, 54]: flow-aligning (**FA**), logrolling (**LR**), logrolling–flow aligning (**LR-FA**), wagging–tumbling (**W-T**), and wagging (**W**). These attractor phase diagrams are consistent with and synthesize earlier 1-d results [53, 54, 55, 68, 20, 64]. We now explain specific features of each type of attractor in Table 1. We give graphical illustrations of the most interesting attractors, starting with steady in-plane 1-d structures.

### I. Steady, in-plane, 1-d attractors.

**FA** steady states: For sufficiently high  $De$  (where the monodomain response is flow-aligning) with in-plane anchoring, steady state structure forms. The major director is aligned in the shear plane throughout the gap, with a boundary layer near each plate that interpolates from the anchoring condition to the preferred midgap alignment angle. In the boundary layers, the order parameters exhibit distortions proportional to the director gradient. These results are consistent with studies of Rey’s group and the authors, and they are omitted.

**LR** steady states: With plate anchoring along the vorticity ( $z$ ) axis, the in-plane attractors at low and intermediate  $De$  are steady and “logrolling,” meaning the major director is oriented with the vorticity axis in the entire shear gap. There is a boundary layer near each plate with order parameter distortions to interpolate from the uniaxial plate condition ( $d_1 > d_2 = d_3$ ) to a fully biaxial distribution ( $d_i$  distinct) that is nearly constant between the boundary layers. These steady structures represent anchoring-dominated elastic distortions, where the flow is not strong enough to impose the monodomain preference for tumbling at the midgap.

**LR-FA** steady states: When  $De$  is sufficiently high, i.e., the flow is strong enough, the midgap response adheres to the monodomain, steady flow-alignment state, Figure 1. To accommodate the logrolling anchoring condition, the structure consists of an interior **FA** gap layer sandwiched between **LR** layers adjacent to each plate. In-plane symmetry constraints impose a nontopological, order-parameter defect phase

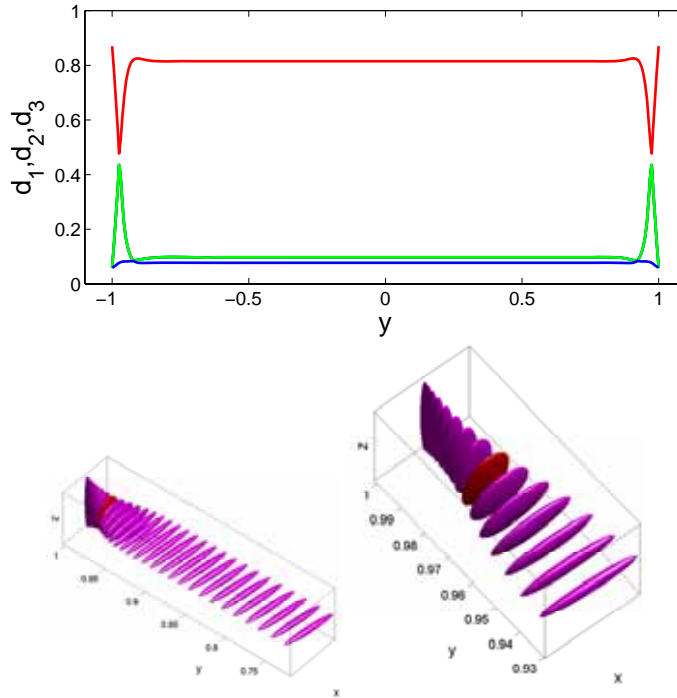


FIG. 2. Nontopological defects in a stationary structure. The order parameters  $d_i$ ,  $i = 1, 2, 3$ , and orientation tensor ellipsoids across the gap for the in-plane **FA-LR** composite steady state with  $De = 6$  and logrolling anchoring conditions.

at the transition site between in-plane and vorticity alignment. These features are illustrated in Figure 2. Note the order parameters  $d_1$  and  $d_2$  collide at the site of transition from vorticity to in-plane alignment, always remaining above  $d_3$ , creating an oblate defect phase (geometrically observed as an oblate second-moment ellipsoid). Prolate spheroids (nondefect phases) arise everywhere else ( $d_1$  strictly greater than  $d_2$ ); the local phases are biaxial ( $d_i$  unequal), except at the plates where we impose the uniaxial equilibrium. Figure 2 shows that the principal axis of  $\mathbf{Q}$  is aligned with the vorticity axis from the plates to the defect and then with an in-plane alignment angle across an interior layer, with  $\phi \sim 6^\circ$  and  $\psi = 0$  at the middle of the gap.

These oblate phase, nontopological defects are shown below to be generic whenever “composite attractors” arise: distinct response functions coexist in the shear gap whenever the physical plate anchoring condition conflicts with a flow-selected internal response function, and the distortional elasticity potential prescribes the spatial interpolation. This “conflict” can be controlled by a combination of anchoring condition and  $De$ , including steady and unsteady structures, in-plane and out-of-plane, 1-d and 2-d tensors, and indeed this is the intuitive basis on which we organize the phase diagrams of Tables 1 and 2.

**II. Unsteady 1-d in-plane attractors.** Just as monodomain attractors undergo a  $De$  transition between steady and unsteady responses (see Figure 1), so do heterogeneous attractors subject to physical anchoring conditions. The first comprehensive documentation of unsteady structure transitions was given by Tsuji and Rey [53, 54, 55], which the authors augmented in subsequent tensor and kinetic studies.

Here we briefly describe the in-plane unsteady attractors, focusing mainly on features that will help illuminate out-of-plane phenomena.

We first note that logrolling plate anchoring conditions and in-plane symmetry impose rigid constraints on unsteady transitions, just as we have seen with steady composite states. That is to say, **LR** states can go unsteady with a continuous director transition only by way of a kayaking orbit, which is disallowed by in-plane symmetry. As Table 1 conveys, in-plane structure attractors with logrolling boundary conditions are always steady! This is a remarkable consequence of anchoring coupled with enforced orientational symmetry. However, these **LR** in-plane confined states will necessarily be extremely sensitive to noise in out-of-plane degrees of freedom; this holds true in all space dimensions and no matter what model one uses! (Note the roll cell steady structures observed by Larson and Mead and modeled by Leal, Klein, et al. are with logrolling plate conditions; we find in unpublished simulations that a small perturbation of the plate anchoring condition leads to breakup of the roll cells.)

**T-W**: From Figure 1, low-to-moderate  $De$  and in-plane symmetry selects unsteady monodomain responses, tumbling **T** at low  $De$  giving way to wagging **W** above a critical  $De$ . At sufficiently low  $De$  together with any in-plane anchoring condition, the midgap tumbles, while the response closer to the plates has to transition to finite oscillations (wagging), which continuously attenuate in amplitude to conform to steady alignment at the plates. Once again, the existence of a composite state leads to nontopological defects at the site of the **T-W** transition; here *the defect phases are transient, local in time as well as space*, forming during the relatively rapid part of the tumbling cycle. This periodic structure attractor has been illustrated in previous studies [54, 20], and thus it is omitted.

**W**: As  $De$  increases from 2 to 3.5, the interior tumbling layer completely vanishes because the monodomain response dominating the interior undergoes the classical **T** to **W** transition. Thus, the entire layer is unsteady with finite oscillations at every interior gap height. These attractors have also been discussed in detail by Rey's group and the authors, and they are omitted. Absent of any "composite" monodomain responses, these unsteady states do not have defects. This comment addresses a basic rule of thumb: nontopological defects arise in 0-, 1-, and 2-d simulations, locally in space and/or time, when there is a transition from one local monodomain response to another, both in steady and unsteady attractors.

We now discuss the stability of these in-plane 1-d attractors to 2-d perturbations, while maintaining in-plane symmetry constraints.

### 3.2. Stability of in-plane 1-d attractors to in-plane 2-d perturbations.

In Table 1, each entry has a  $-1$  for stability and  $-2$  for instability to 2-d perturbations. Thus, at  $De$  and anchoring conditions that indicate instability, there is *coexistence of 1-d and 2-d heterogeneous attractors*. The overall stability picture is relatively straightforward for all three anchoring conditions:

- for sufficiently low and high  $De$ , the 1-d attractors are robust to 2-d perturbations, whereas
- at intermediate  $De$ , full 2-d morphology develops from noisy perturbations of the unstable 1-d attractors.

Higher resolution details depend on anchoring conditions. For anchoring in the shear plane, the monodomain  $De$  cascade is a faithful predictor of the  $De$  structure cascades: the 1-d structure transitions are longwave in  $y$ , and the 1-d to 2-d transitions are also associated with longwave  $y, z$ -dependent structure. This explains, in

retrospect, why the early focus on orientational monodomain dynamics was so successful.

The logrolling anchoring condition together with in-plane symmetry has a far more dramatic effect. Vorticity alignment suppresses all unsteady limit cycles, independent of whether the attractor is 1-d or 2-d. This is intuitively clear: the major director cannot smoothly transition from the  $z$ -axis at the plates to the kayaking limit cycle (whose director violates in-plane symmetry), so it remains pinned along the vorticity axis. As one can glean from a comparison of Tables 1 and 2, these responses are highly sensitive and go away if symmetry is broken (either of the anchoring condition or the interior constraints).

Since 2-d attractors require significant detail to explain and visualize and the most physically relevant structures are with full tensor degrees of freedom, we defer 2-d descriptions to full tensor simulations.

**3.3. Table 2: Full tensor, 1-d heterogeneous attractors and their stability to 2-d perturbations.** The next simulation results, collected in Table 2, convey the stability of Table 1 solutions with respect to out-of-plane orientational degrees of freedom, thereby extending information in the monodomain diagram, Figure 1, to 1 and 2 space dimensions. We conclude that instability to out-of-plane orientation is a longwave instability; the historical studies of monodomain dynamical systems are therefore faithful indicators of  $De$  transitions with physical boundary conditions. The caveat to this general statement is that the anchoring condition and strength of the distortional elasticity potential can overwhelm flow selection criteria in the middle of the gap; an example of this was given above for logrolling anchoring with in-plane symmetry.

The diverse 1-d, full tensor, structure attractors (Table 2 entries) have been a principal focus of the past several years of modeling and simulation. Almost all reports have shown that fixed  $De$  attractors and  $De$ -dependent transitions occur with a finite lengthscale of gradient structure in the gap ( $y$  direction), independent of attractor type (steady and unsteady, regular or chaotic). Table 2 gives a benchmark on the literature for the continuum model and then conveys results of the new study of stability to two space-dimensional perturbations.

We begin with descriptions of representative 1-d full tensor attractors in Table 2. These structure attractors have been described in several ways (cf. [53, 54, 55, 31, 13, 14, 49, 68, 20, 63, 64, 21]); we adopt these descriptions and present new graphical illustrations that distinguish among 1-d structure attractors and describe key features of 2-d morphologies.

In Table 2, 1-d full-tensor attractors are classified according to their monodomain responses at each spatial site; as with in-plane attractors, the structure responses are either uniform across the gap or form three layers, one in the interior and another response near each plate. In addition to the in-plane monodomain responses discussed above, additional limit cycles associated with full orientational degrees of freedom are labeled as follows:  $\mathbf{K}_1$  denotes the classical Larson–Ottinger kayaking attractor for which the major director rotates about the vorticity axis;  $\mathbf{K}_2$  denotes a tilted kayaking attractor, which comes in pairs due to reflection symmetry about the shear plane, for which the major director rotates about an axis tilted between the vorticity axis and shearing plane; and  $\mathbf{CH}$  denotes a chaotic attractor which typically jumps erratically between both types of kayaking limit cycles. The out-of-plane steady response is labeled  $\mathbf{OS}$ , where the primary director is tilted between the shear plane and vorticity axis.

As with Table 1, the most dramatic differences due to anchoring in Table 2 arise with the logrolling condition, which promotes symmetric  $\mathbf{K}_1$  kayaking orbits instead of tilted  $\mathbf{K}_2$  orbits that are promoted by any other anchoring condition.

### I. Steady full tensor, 1-d attractors and stability to 2-d perturbations.

At sufficiently low  $De$ , distortional elasticity overwhelms the flow, and steady structures dominate. We omit these attractors since they are quite similar to the steady structures explored in the asymptotic low  $De$  regime by the authors [17, 20, 63, 8]. Likewise, at high  $De$ , the flow imposes a steady alignment response in the interior, and steady structures prevail. The details of structure vary with the anchoring condition (in-plane, logrolling, or tilted) and  $De$ , which have already been documented in results of Rey's group and the authors. We also omit these steady 1-d structure figures to save space. They have similar features to in-plane steady states: the degree of gradient structure depends at high  $De$  on the relative mismatch between the monodomain flow-alignment preference and the anchoring condition; at very low  $De$  (not shown in Table 2) and the  $Er = 1000$  imposed here, distortional elasticity overwhelms the preference of the nematic liquid to kayak and arrests the dynamics. If the anchoring condition conflicts with the midgap steady alignment, a nontopological defect phase allows the orientation tensor to interpolate between them (cf. the **LR-FA** steady structure shown earlier).

The steady **FA** 1-d structures at high  $De$  are all stable to 2-d perturbations. The simulations are not very enlightening, in that the Legendre–Fourier modal amplitudes are given an initial noisy amplitude distribution superimposed on the steady 1-d attractor, and then the 2-d modal amplitudes all decay exponentially to zero. Rather than show this linearized stability behavior, we defer the illustration to the more interesting unsteady attractors which also share linearized 2-d stability.

### II. Unsteady out-of-plane 1-d attractors and their (in)stability to 2-d perturbations.

Recall from Figure 1 that full-tensor monodomain limit cycles are out-of-plane (i.e., kayaking) at low  $De$ ; tumbling in-plane orbits are unstable to out-of-plane degrees of freedom. Then a remarkable  $De$  sequence unfolds, with coexistence of symmetric and tilted kayaking orbits, period-doubling sequences to chaos from the tilted kayaking orbits, and then a regularizing sequence back to periodic tilted kayaking and finally to steady flow alignment. The 1-d structure responses inherit these dynamical features especially at early times after the plates are set into motion, but plate anchoring imposes conflicts with the interior response functions, leading to space-time attractors that we illustrate next. This overview of the full tensor, 1-d attractor phase diagram versus  $De$  for various anchoring conditions has not appeared in the literature, so it is worth some attention at this junction.

**$\mathbf{K}_2$ - $\mathbf{K}_1$**  unsteady 1-d states: This composite attractor arises for all anchoring conditions *except logrolling* at low  $De$ . The interior response is consistent with monodomains in weak shear, namely the classical  $\mathbf{K}_1$  kayaking orbit. However, the plate boundary condition, unless it is logrolling, is inconsistent with kayaking based on symmetry. The compromise response is the  $\mathbf{K}_2$  tilted kayaking orbit in layers near the plates, with  $\mathbf{K}_1$  limit cycles in the interior of the gap. This composite phase is the out-of-plane analogue of the tumbling-wagging composite attractor; indeed, the projections onto the shear plane of kayaking and tilted kayaking are tumbling and wagging, respectively. Again, the transition between finite and continuous rotations in the shear gap spawns nontopological, oblate phase defects that are local in space and periodic in time. Figure 3 conveys salient features: the order parameters  $d_i(y, t)$  indicate strong defocusing events near the plates where  $d_1$  and  $d_2$  periodically collide,

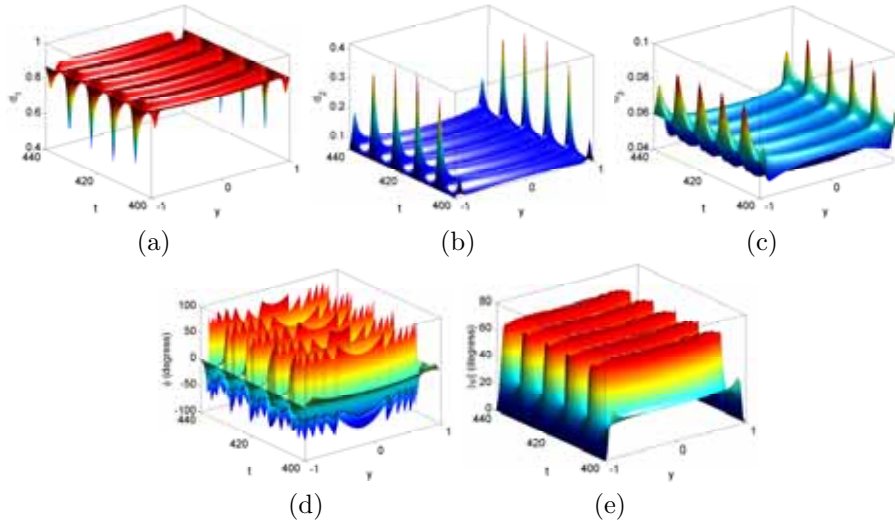


FIG. 3. Features of the unsteady composite  $\mathbf{K}_2\text{-}\mathbf{K}_1$  attractor at  $De = 2$  with tangential anchoring. (a) The principal eigenvalue  $d_1$  of the second-moment tensor; (b) the second eigenvalue  $d_2$  of  $\mathbf{M}$ ; (c) the smallest eigenvalue  $d_3$  of  $\mathbf{M}$ ; (d) the in-plane angle  $\phi$  of the major director; (e) the absolute value  $|\psi|$  of the angle between the major director and the shear plane.

yet remain bounded above  $d_3$ , leading to periodic formation of a local oblate defect phase near each plate; the major director’s in-plane angle  $\phi$  and out-of-plane angle  $\psi$  indicate kayaking layers near the plates and a tilted kayaking layer in the interior, but it is difficult to glean this property without careful inspection. Alternatively, Figure 4, top row, shows the major director dynamics sitting at two specific heights in the shear gap, clearly conveying the midgap ( $y = 0$ ) kayaking orbit versus the tilted kayaking orbit near the top plate. To see the defect event more clearly, the bottom graphic of Figure 4 shows a time series of the orientation tensor ellipsoids across the gap, where the time sequence is chosen to capture the oblate defect phase onset, formation, and dissolution.

**3.4. 1-d  $\mathbf{K}_2\text{-}\mathbf{K}_1$  attractors at low  $De$ ; stability to 2-d perturbations.**

We now illustrate the results of Table 2 regarding the *stability of low  $De$ , unsteady, kayaking structure attractors to 2-d perturbations*. We begin with a snapshot of the  $De = 2$  attractor above for tangential anchoring; that data is then used to populate initial conditions for a full 2-d simulation, with superimposed noise on the Legendre–Fourier amplitudes  $a_{k,m}$ . Figure 5 shows the results: the exponential convergence to zero of the randomly chosen 2-d amplitude function,  $a_{7,6}(t)$ , where all other 2-d amplitudes (not shown) are behaving the same; and one snapshot of the corresponding 2-d array of orientation tensor ellipsoids after the 2-d transients have died out, clearly showing zero gradients in  $z$ . There is no generation of higher space-dimensional modes throughout the dynamics of the 1-d unsteady attractors, including during the local defect generation events. These stability results are typical of all attractors labeled in Tables 1 and 2 as stable to 2-d perturbations.

**3.5. 1-d  $\mathbf{K}_2\text{-}\mathbf{K}_1$  attractors at moderate  $De$ ; instability to weak 2-d morphology and chaotic dynamics.** Next, we simply increase the  $De$  from 2 to 3.75, retaining tangential anchoring. The 1-d  $\mathbf{K}_2\text{-}\mathbf{K}_1$  attractor persists in the confined 1-d simulations. We then repeat the stability simulation carried out at  $De = 2$ . As shown

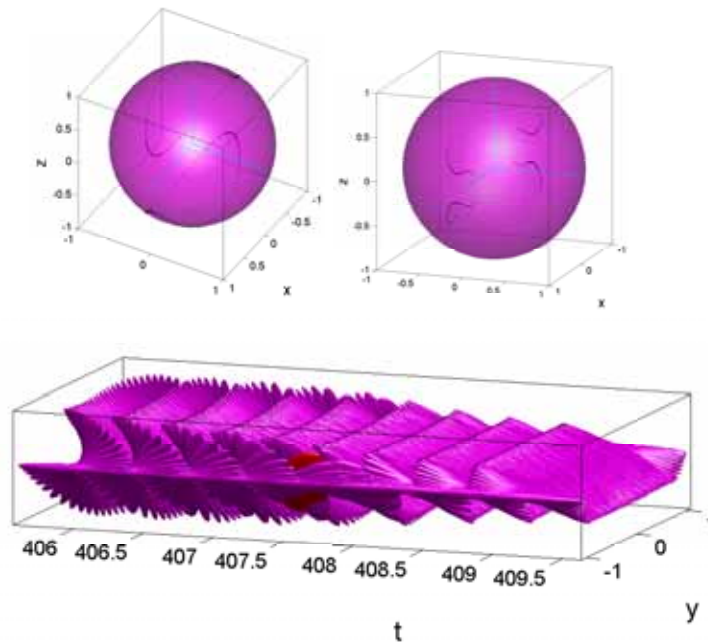
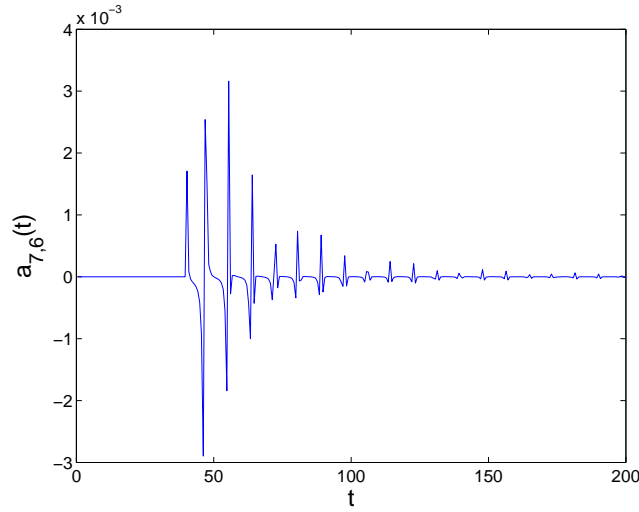


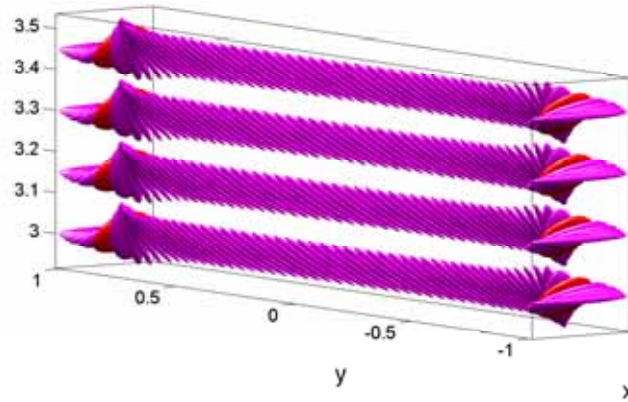
FIG. 4. Features of the 1-d unsteady composite  $\mathbf{K}_2\text{-}\mathbf{K}_1$  attractor at  $De = 2$  with tangential anchoring. Top row: the major director kayaking orbit at the midgap,  $y = 0$ ; the tilted kayaking orbit at  $y = 0.95$  near the top plate. Bottom row: the second-moment tensor ellipsoids across the gap in a time sequence that captures the oblate defect phase formation and breakup near the plates.

in Figure 6, the 2-d amplitude functions (we choose  $a_{9,6}(t)$  for this simulation) do not converge back to zero, and instead the amplitudes saturate to nonzero dynamics to form a transient 2-d morphology. The Legendre–Fourier modal amplitudes remain relatively small (compared to other 2-d morphologies shown below), yet they take on the same signatures of chaotic 0- and 1-d attractors. Thus, we find the  $De$  transition to chaotic dynamics occurs at reduced  $De$  in 2 space dimensions! This is consistent with our recent comparison of 0-d monodomain and 1-d heterogeneous chaotic attractors, where the measures of chaos such as positive Lyapunov exponents are enhanced by spatial degrees of freedom [21]. Figure 7 shows two representative snapshots of the weak 2-d morphology: the order-parameter diagnostic  $s - \beta = d_1 - d_2$  drops only by 10% from the equilibrium value at the plates, so that the orientation is a nearly uniaxial, prolate phase across  $y$ - $z$  and there are no defect structures in these snapshots; the out-of-plane angle  $\psi$  of the major director suggests a tilted kayaking phase across  $y$ - $z$ , with axis of symmetry close to the shear plane. This is confirmed only by producing local monodomain orbits per spatial site, which we omit due to space limitations since we will give such an illustration below for another 2-d spatio-temporal attractor. Thus, in addition to development of 2-d morphology, the local monodomain response functions have changed dramatically, replacing kayaking around the vorticity axis by erratic dynamics and jumping between tilted kayaking and kayaking orbits.

**CH** unsteady 1-d states: We now raise  $De$  to 4.5 and switch to normal anchoring to illustrate a different boundary condition in the phase diagram, Table 2. From



(a)



(b)

FIG. 5. Stability of the 1-d  $\mathbf{K}_2\text{-}\mathbf{K}_1$  attractor at  $De = 2$  with tangential anchoring. (a) The dynamics of a randomly chosen 2-d Fourier-Legendre amplitude function,  $a_{7,6}(t)$ , from noisy initial data superimposed on a snapshot of the 1-d attractor. (b) A snapshot of the orientation tensor ellipsoids after transients have passed from the 2-d perturbation, showing a return to stable 1-d morphology.

Table 2, the 1-d attractor is temporally chaotic, depicted in Figure 8. We choose in (a)–(c) to show the primary order parameters,  $d_i$ , of the second-moment tensor; one can see intermittent oblate defect phases ( $d_1$  and  $d_2$  collide, bounded above  $d_3$ ) that are local in space and time. The surface plots (d)–(e) of the major director angles show the chaotic signature across the shear gap where the major director ranges all over the sphere. To see the local monodomain signature of chaos, in (f) we show the orbit of the major director at the midgap location,  $y = 0$ , indicating the classical chaotic orbit of a random jump between kayaking and tilted kayaking orbits. To see the spatial morphology at any given time, in (g) we show the 1-d distribution of orientation tensor ellipsoids in a time sequence chosen to capture the defect phase. These 1-d chaotic attractor features are consistent with results in [21], where flow is

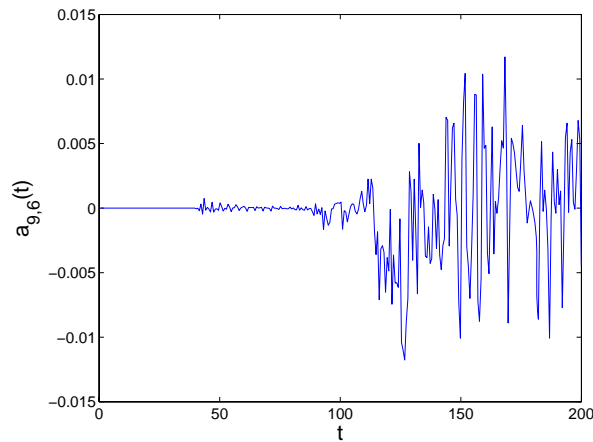


FIG. 6. *Instability of the 1-d  $\mathbf{K}_2$ - $\mathbf{K}_1$  attractor at  $De = 3.75$  with tangential anchoring. The dynamics of one randomly chosen Fourier-Legendre amplitude function,  $a_{9,6}(t)$ , from noisy initial data superimposed on a snapshot of the 1-d attractor.*

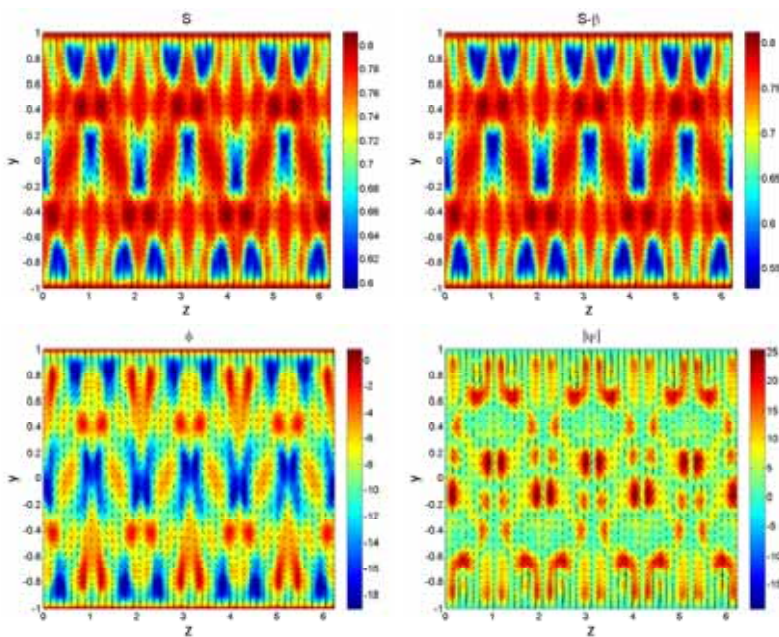


FIG. 7. *A snapshot of the transient 2-d morphology at  $De = 3.75$  with tangential anchoring at  $t = 200$ , corresponding to Figure 6. The top two panels give the order parameter  $s = d_1 - d_3$ ,  $s - \beta = d_1 - d_2$ , while the bottom row gives the major director angles  $\phi, |\psi|$  in the  $y$ - $z$  domain. The superimposed line segments represent the projections of the major director onto the  $y$ - $z$  plane, which reduce to points along  $y = -1, 1$  due to tangential anchoring.*

coupled, indicating that at least in 1 dimension, secondary flow is perturbative on the basic orientational response functions. The temporal statistics at a given gap height are chaotic, while a Fourier decomposition in space at any fixed time shows a long-to-intermediate wavelength structure.

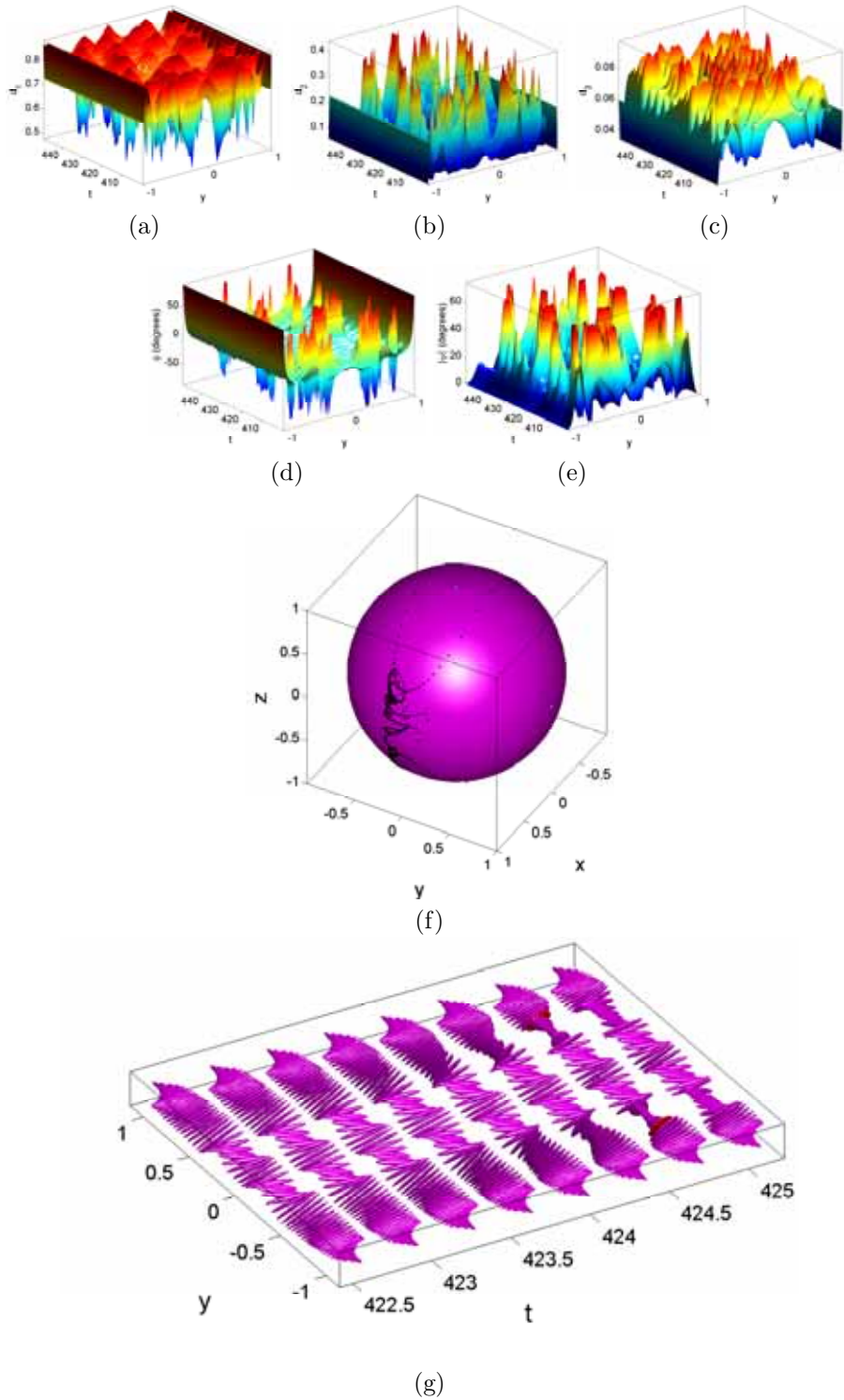


FIG. 8. The 1-d chaotic attractor for  $De = 4.5$  and normal anchoring. (a)–(c) The ordered eigenvalues  $0 \leq d_1 \leq d_2 \leq d_3 \leq 1$  of the second-moment tensor. (d) In-plane ( $\phi$ ) and (e) out-of-plane ( $|\psi|$ ) angles of the major director. (f) The major director orbit at  $y = 0$ . (g) Time sequence of the orientation ellipsoids across the gap.

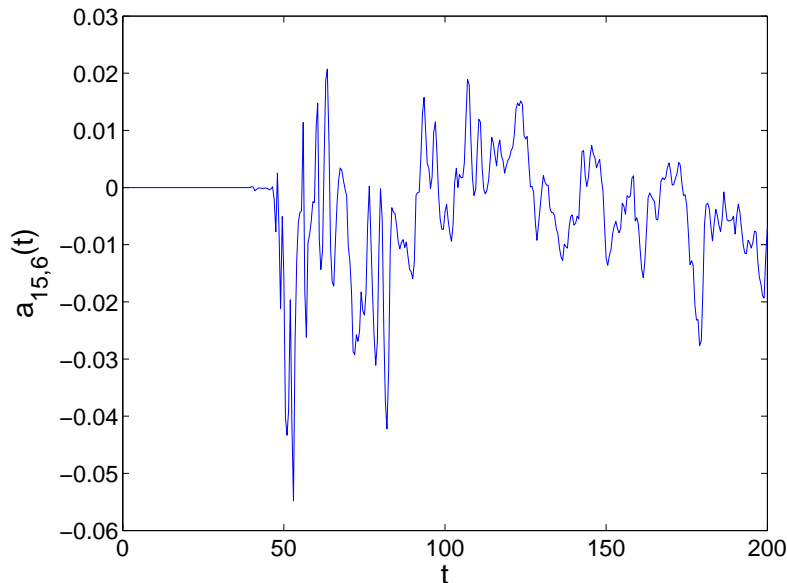


FIG. 9. Dimensional instability of the 1-d chaotic attractor at  $De = 4.5$  with normal anchoring. The dynamics of the randomly chosen Fourier–Legendre amplitude function  $a_{15,6}(t)$  after noisy initial data is superimposed on a snapshot of the 1-d attractor.

**3.6. 1-d chaotic attractors at intermediate  $De$ ; instability to strong 2-d morphology and persistent chaotic dynamics.** We use this entry of Table 2 to highlight a generic observation regarding 2-d perturbations. When the 1-d attractor is temporally chaotic, we always find the following:

- Instability to 2-d perturbations: Figure 9 shows the growth and persistence of the 2-d modal amplitude  $a_{15,6}$  with higher amplitudes in all modal amplitudes (not shown) than the previous 2-d structure at  $De = 3.75$ .
- Convergence to a strong 2-d morphology at each snapshot: Figure 10 shows strong 2-d gradients and structure in the order parameters and director angles, where we have superimposed the  $y$ - $z$  projection of the major director in each panel to see correlations between order parameter and director gradient features. The diagnostic  $s - \beta = d_1 - d_2$  shows a higher density of 2-d oblate defect phases, which are further visualized in the 2-d array of orientation tensor ellipsoids around the site  $(y, z) = (-0.6, 4.5)$ . Thus, the 1-d nontopological defect phases persist in 2 dimensions and expand into 2-d domains.
- Persistence of chaotic dynamics, which can be seen from the dynamics of the modal amplitudes: The release of chaotic responses into higher space dimensions does not arrest the irregular dynamics.

**3.7. 1-d chaotic attractors with tilted anchoring; instability to 2-d chaotic attractors.** Next, we retain  $De = 4.5$  but change the anchoring conditions to tilted (between the shear plane and vorticity axes):  $\mathbf{n}_0 = \frac{1}{\sqrt{3}}(1, 1, 1)$ . The amplitude functions  $a_{k,m}(t)$  again grow and saturate to finite values, omitted here since they are similar to earlier figures. Figure 11 shows the 2-d morphology snapshot for comparison with the normal anchoring results of Figure 10. This example illus-

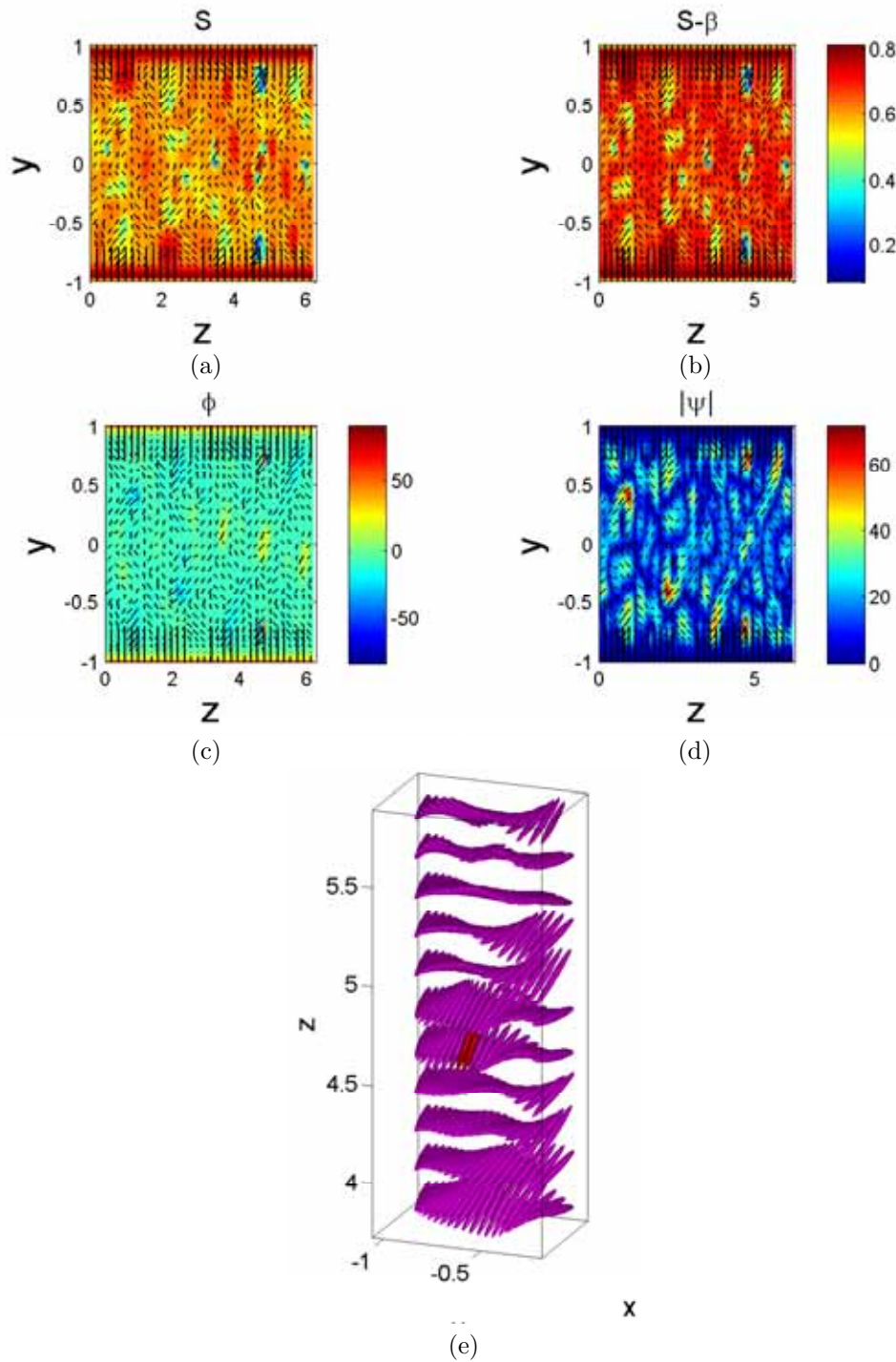


FIG. 10. A snapshot of the 2-d morphology that evolves from the unstable chaotic 1-d attractor at  $De = 4.5$  with normal anchoring, corresponding to the full collection of 2-d amplitude functions sampled in Figure 9. (a), (b) The order parameters  $s, s-\beta$ ; (c), (d) the major director angles  $\phi, |\psi|$ ; (e) the orientation tensor ellipsoids around the site  $(y, z) = (-0.6, 4.5)$  which illustrate 2-d gradients and local 2-d oblate defect domains. The superimposed line segments are the  $y$ - $z$  projections of the major director, which are normal to the plates.

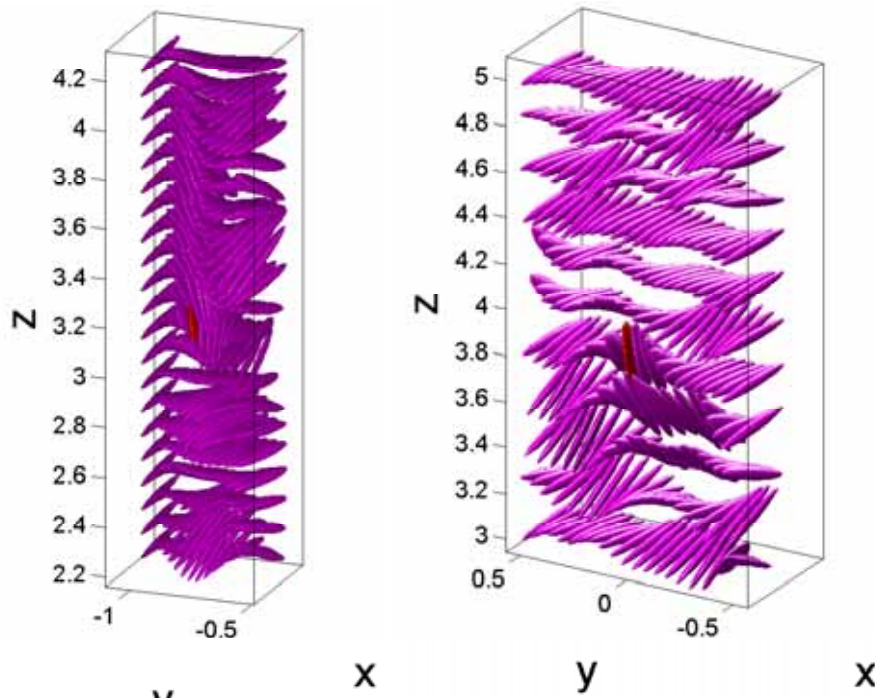


FIG. 11. Two snapshots of the 2-d morphology that evolves from the unstable chaotic 1-d attractor at  $De = 4.5$  with tilted anchoring. The orientation tensor ellipsoids are blown up at different sites in each snapshot to better resolve the morphology,  $(y, z) = (-0.8, 3.2)$  and  $(0, 4)$ , illustrating strong 2-d gradients and a high density of local 2-d oblate defect domains.

trates the role of anchoring when the dynamics is chaotic: the major gradient and dynamical features are preserved, but the locations of nontopological defect domains are shifted.

**$\mathbf{K}_1$  unsteady 1-d states:** When the anchoring conditions are logrolling, there is a *dramatic* difference in the heterogeneous response functions versus  $De$ , as seen in Table 2. For example, Table 2 indicates for  $De = 4.5$  that there are chaotic 1-d response functions for all other anchoring conditions, whereas logrolling induces a periodic, kayaking attractor across the shear gap. Figure 12 shows the 1-d  $\mathbf{K}_1$  attractor features. Note that since the local monodomain response is uniformly kayaking across the shear gap, there are no defect phases:  $d_1 > d_2$  uniformly in  $y, t$ . The response is periodic, and the orbit of the major director at  $y = 0$  illustrates classical kayaking. The ellipsoid time series across the gap does not reflect any defect phases.

**3.8. 1-d  $\mathbf{K}_1$  attractor with logrolling anchoring; instability to 2-d morphology with chaotic dynamics.** The kayaking 1-d attractor at  $De = 4.5$  for logrolling boundary conditions is quite sensitive to 2-d perturbations. We omit the 2-d amplitude function growth since it is similar to other unstable time series. A strong 2-d morphology develops, with local oblate defect domains shown in Figure 13. The dynamics is no longer periodic, so that the instability to 2-d degrees of freedom coincides with a periodic to chaotic dynamical transition. Note that, at slightly higher  $De$ , Table 2 shows that the 1-d confined simulations are chaotic. Taken together, the 2-d attractors with irregular dynamics clearly show a significant disparity

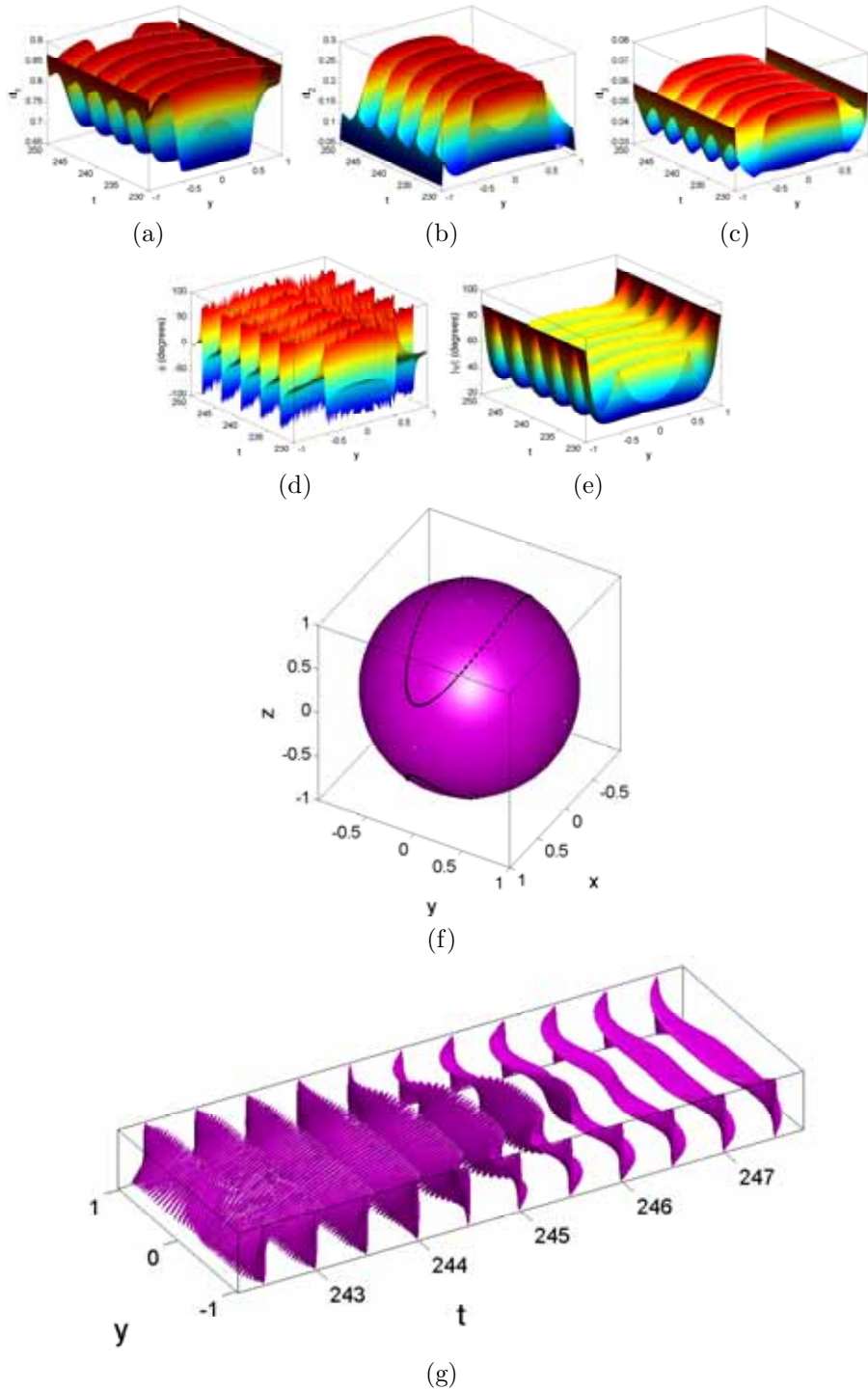


FIG. 12. The 1-d kayaking ( $\mathbf{K}_1$ ) attractor for  $De = 4.5$  and vorticity anchoring. (a)–(c) The ordered eigenvalues  $0 \leq d_1 \leq d_2 \leq d_3 \leq 1$  of the second-moment tensor. (d) In-plane ( $\phi$ ) and (e) out-of-plane ( $|\psi|$ ) angles of the major director. (f) The major director orbit at  $y = 0$ . (g) Time sequence of the orientation ellipsoids across the gap.

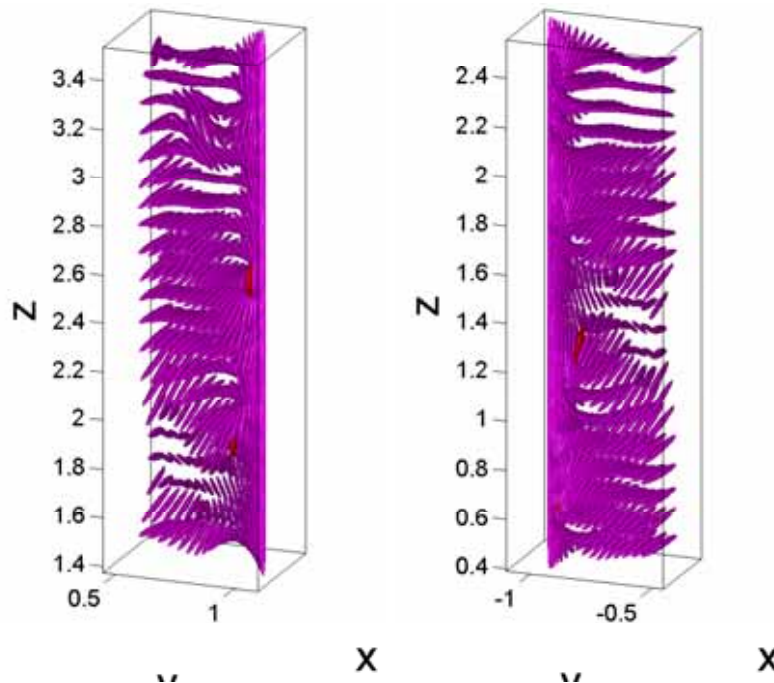


FIG. 13. A snapshot of the 2-d morphology that evolves from the unstable 1-d  $\mathbf{K}_1$  attractor at  $De = 4.5$  with logrolling anchoring. The orientation tensor ellipsoids are resolved around two sites,  $(y, z) = (0.9, 2.6)$  and  $(-0.9, 1.4)$ , which illustrate strong 2-d gradients and local 2-d oblate defect domains.

with confined 1-d simulations in terms of the  $De$  transitions and in fully 2-d gradient morphology.

**4. Conclusion.** A comprehensive numerical study of orientational morphology induced by pure shear flow has been presented, focusing on the Deborah number cascade in a hierarchy of 0, 1, and 2 space dimensions, for a range of plate anchoring conditions and for a fixed strength of the distortional elasticity potential. The spectral-Galerkin algorithm has produced benchmarks on the model with respect to previous results for 1-d morphology, achieved with initial data that populates only the Legendre basis along the flow-gradient direction. We recover the diversity of previously reported steady and unsteady 1-d morphology attractors, including in-plane and full orientation tensor degrees of freedom, tensor and kinetic models, and flow-imposed and flow-coupled systems, for various plate orientational anchoring conditions [53, 54, 63, 64, 49, 31, 68, 20, 21]. When compiled into Deborah number cascades at a fixed Ericksen number for various wall anchoring conditions, 1-d attractor phase diagrams qualitatively match and extend these previous model predictions to larger parameter ranges.

The main new results presented are the numerical stability of 1-d sheared morphology to 2-d perturbations in the flow-gradient and vorticity directions and a description of the 2-d morphologies that arise from unstable attractors. We find that widely observed time-periodic, 1-d structure attractors at low-to-moderate  $De$  are stable to 2-d perturbations, except when the  $De$  is near the periodic-to-chaotic transition which is *lowered* with 2-d morphology. These results include diverse structure

attractors that arise for the various anchoring conditions, primarily involving kayaking in interior layers and tilted kayaking in layers extending to the plates, or in the special case of vorticity-anchoring, where the response is kayaking everywhere in the shear gap. As  $De$  is raised to values where monodomains and 1-d attractors undergo period-doubling transitions to chaos, instability to 2-d morphology develops; we repeat that the  $De$  transition to chaos is lowered in the presence of 2-d morphology. As  $De$  increases, again consistent with the 0-d and 1-d phase diagram predictions, chaotic responses regularize to periodic and then steady structure attractors, and the structures stabilize and return to robust 1-d morphology.

We find that logrolling (vorticity-aligned) anchoring selects the most distinct attractors and  $De$  cascade with respect to other anchoring conditions. In particular, kayaking attractors dominate at low to moderate  $De$ , and the transition to chaotic, 2-d attractors is delayed relative to other anchoring conditions. With in-plane symmetry, logrolling anchoring has the most dramatic consequence, arresting all dynamics in the attracting states. Such predictions are therefore not to be trusted for physical applications.

We further have illuminated the generic feature of nontopological defects, having to do with order-parameter degeneracy instead of director winding number topology. These order-parameter defects arise whenever there are composite attractors consisting of distinct types of monodomain response in complementary layers in the shear gap, such as kayaking in an interior layer and tilted kayaking in layers extending from the plates, or even in steady structures which are logrolling at the walls and flow-aligning in the interior of the shear gap. These defects correspond to a degeneracy in which the leading two eigenvalues of the orientation tensor collide, meaning a loss of uniqueness of the principal axis of orientation. We have illustrated the genericity of these defects in steady and unsteady, in-plane and full tensor, and 1-d and 2-d structure attractors.

It is appropriate that we mention the relationship between our results and those of the Leal group [29] on *flow-coupled* 2-d simulations with a tensor orientation model and Marrucci–Greco distortional elasticity potential. Leal’s group has focused exclusively on logrolling boundary conditions; in the low  $De$  regime with a moderate  $Er$  similar to our study here, they reveal a detailed description of the flow feedback phenomenon of steady roll cells accompanied by a full 2-d morphology. Our study suppresses hydrodynamic modes in the secondary velocity fields  $(v_y, v_z)(y, z)$  that yield roll cells; when restricted to vorticity alignment at both plates as in [29] and low  $De$ , our model predicts stable 1-d steady orientational morphologies. This is represented for confined in-plane tensor degrees of freedom in Table 1, row 3; one sees that the transition to 2-d morphology arises at a moderate Deborah number between  $De = 2$  and 3.5. For out-of-plane simulations, Table 2, row (1, 1, 1), shows that  $De = 2$  yields a stable 1-d unsteady kayaking attractor. Not shown in Table 2, row (0, 0, 1), is the low  $De$  limit, which reveals steady **LR** 1-d structures that are stable to 1-d perturbations. The natural conclusion from the flow-imposed and flow-coupled comparison is that flow-coupling preserves steady structure, but the weak nonlinear flow feedback leading to steady roll cells generates a correspondingly weak 2-d orientational morphology. Furthermore, we surmise that the nonlinear flow-induced orientational morphology is responsible for the topological defects identified in [29], since none of our pure shear-imposed 2-d morphologies has director defects! This and related issues are the focus of present studies in our group for flow-coupled 2-d simulations, both for tensor and kinetic models.

Finally, we mention closely related materials science applications toward which

this study contributes. Numerical databases for sheared orientational distributions of nanorod dispersions have been mapped to effective film properties in a series of papers [60, 66, 59, 61, 64]. With these tools, the results of the present paper are also applicable to determine heterogeneous property tensors, given known material properties of the particle phase and solvent. These applications are especially interesting for 2-d sheared property tensors, which have not previously been explored.

## REFERENCES

- [1] K. ASOKAN, C. V. A. KUMAR, J. DASAN, K. RADHAKRISHNAN, K. S. KUMAR, AND T. R. RAMAMOCHAN, *Review of chaos in the dynamics and rheology of suspensions of orientable particles in simple shear flow subject to an external periodic force*, J. Non-Newtonian Fluid Mech., 129 (2005), pp. 128–142.
- [2] D. BAALSS AND S. HESS, *The viscosity coefficients of oriented nematics and nematics discotic liquid crystals, affine transformation model*, Z. Naturforsch. A, 43 (1988), pp. 662–670.
- [3] D. BAALSS AND S. HESS, *Nonequilibrium molecular-dynamics studies on the anisotropic viscosity of perfectly aligned nematic liquid crystals*, Phys. Rev. Lett., 57 (1986), pp. 86–89.
- [4] W. R. BURGHARDT, *Oscillatory shear flow of nematic liquid crystals*, J. Rheol., 35 (1991), pp. 49–62.
- [5] W. R. BURGHARDT, *Molecular orientation and rheology in sheared lyotropic liquid crystalline polymers*, Macromol. Chem. Phys., 199 (1998), pp. 471–488.
- [6] E. CHOATE, Z. CUI, AND M. G. FOREST, *Linear viscoelasticity of heterogeneous nematic polymers*, Rheol. Acta, to appear.
- [7] E. CHOATE AND M. G. FOREST, *A classical problem revisited: Rheology of nematic polymer monodomains in small amplitude oscillatory shear*, Rheol. Acta, 46 (2006), pp. 83–94.
- [8] Z. CUI, M. G. FOREST, Q. WANG, AND H. ZHOU, *On weak plane Couette and Poiseuille flows of rigid rod and platelet ensembles*, SIAM J. Appl. Math., 66 (2006), pp. 1227–1260.
- [9] Z. CUI AND Q. WANG, *A continuum model for flows of cholesteric liquid crystal polymers and permeation flows*, J. Non-Newtonian Fluid Mech., 138 (2006), pp. 44–61.
- [10] P. G. DE GENNES AND J. PROST, *The Physics of Liquid Crystals*, Oxford University Press, London, 1993.
- [11] M. DOI, *Molecular dynamics and rheological properties of concentrated solutions of rod-like polymers in isotropic and crystalline phases*, J. Polym. Sci.: Polym. Phys. Ed., 19 (1981), pp. 229–243.
- [12] V. FARAONI, M. GROSSO, S. CRESCITELLI, AND P. L. MAFFETTONE, *The rigid-rod model for nematic polymers: An analysis of the shear flow problem*, J. Rheol., 43 (1999), pp. 829–843.
- [13] J. J. FENG, G. SGALARI, AND L. G. LEAL, *A theory for flowing nematic polymers with orientational distortion*, J. Rheol., 44 (2000), pp. 1085–1101.
- [14] J. J. FENG, J. TAO, AND L. G. LEAL, *Roll cells and disclinations in sheared nematic polymers*, J. Fluid Mech., 449 (2001), pp. 179–200.
- [15] M. G. FOREST AND Q. WANG, *Monodomain response of finite-aspect-ratio macromolecules in shear and related linear flows*, Rheol. Acta, 42 (2003), pp. 20–46.
- [16] M. G. FOREST, Q. WANG, AND H. ZHOU, *Exact banded patterns from a Doi-Marrucci-Greco model of nematic liquid crystal polymers*, Phys. Rev. E (3), 61 (2000), pp. 6655–6662.
- [17] M. G. FOREST, Q. WANG, H. ZHOU, AND R. ZHOU, *Structure scaling properties of confined nematic polymers in plane Couette cells: The weak flow limit*, J. Rheol., 48 (2004), pp. 175–192.
- [18] M. G. FOREST, Q. WANG, AND R. ZHOU, *The weak shear phase diagram for nematic polymers*, Rheol. Acta, 43 (2004), pp. 17–37.
- [19] M. G. FOREST, Q. WANG, AND R. ZHOU, *The flow-phase diagram of Doi-Hess theory for sheared nematic polymers II: Finite shear rates*, Rheol. Acta, 44 (2004), pp. 80–93.
- [20] M. G. FOREST, R. ZHOU, AND Q. WANG, *Kinetic structure simulations of nematic polymers in plane Couette cells. II: In-plane structure transitions*, Multiscale Model. Simul., 4 (2005), pp. 1280–1304.
- [21] M. G. FOREST, R. ZHOU, AND Q. WANG, *Microscopic-macroscopic simulations of rigid-rod polymer hydrodynamics: Heterogeneity and rheochaos*, Multiscale Model. Simul., 6 (2007), pp. 858–878.
- [22] A. FURUKAWA AND A. ONUKI, *Spatio-temporal structures in sheared polymer systems*, Phys. D, 205 (2005), pp. 195–206.
- [23] A. GOPINATH, R. C. ARMSTRONG, AND R. A. BROWN, *Observations on the eigenspectrum of the linearized Doi equation with application to numerical simulations of liquid crystal*

- suspensions*, J. Chem. Phys., 121 (2004), pp. 6093–6098.
- [24] M. J. GREEN, R. A. BROWN, AND R. C. ARMSTRONG, *Nonhomogeneous shear flow in concentrated liquid-crystalline solutions*, Phys. Fluids, to appear.
- [25] M. GROSSO, S. CRESCITELLI, E. SOMMA, J. VERMANT, P. MOLDENAERS, AND P. L. MAFFETTONE, *Prediction and observation of sustained oscillations in a sheared liquid crystalline polymer*, Phys. Rev. Lett., 90 (2003), 098304.
- [26] M. GROSSO, P. L. MAFFETTONE, P. HALIN, R. KEUNINGS, AND V. LEGAT, *Flow of nematic polymers in eccentric cylinder geometry: Influence of closure approximations*, J. Non-Newtonian Fluid Mech., 94 (2000), pp. 119–134.
- [27] S. HESS, *Fokker-Planck-equation approach to flow alignment in liquid crystals*, Z. Naturforsch. A, 31 (1976), pp. 1034–1037.
- [28] D. H. KLEIN, *Dynamics of a Model for Nematic Liquid Crystalline Polymers in Planar Shear Flow*, Ph.D. thesis, University of California, Santa Barbara, CA, 2007.
- [29] D. H. KLEIN, C. J. GARCÍA-CERVERA, H. D. CENICEROS, AND L. G. LEAL, *Ericksen number and Deborah number cascade predictions of a model for liquid crystalline polymers for simple shear flow*, Phys. Fluids, 19 (2007), 023101.
- [30] M. KROGER AND P. ILG, *Derivation of Frank-Ericksen elastic coefficients for polydomain nematics from mean-field molecular theory for anisotropic particles*, J. Chem. Phys., 127 (2007), 034903.
- [31] R. KUPFERMAN, M. KAWAGUCHI, AND M. M. DENN, *Emergence of structure in a model of liquid crystalline polymers with elastic coupling*, J. Non-Newtonian Fluid Mech., 91 (2000), pp. 255–271.
- [32] N. KUZUU AND M. DOI, *Constitutive equation for nematic liquid crystals under weak velocity gradient derived from a molecular kinetic equation I*, J. Phys. Soc. Japan, 52 (1983), pp. 3486–3494.
- [33] R. G. LARSON AND D. W. MEAD, *The Ericksen number and Deborah number cascade in sheared polymeric nematics*, Liq. Cryst., 15 (1993), pp. 151–169.
- [34] R. G. LARSON AND H. C. OTTINGER, *Effect of molecular elasticity on out-of-plane orientations in shearing flows of liquid crystalline polymers*, Macromolecules, 24 (1991), pp. 6270–6282.
- [35] F. M. LESLIE, *Theory of flow phenomena in liquid crystals*, in Advances in Liquid Crystals, Vol. 4, G. H. Brown, ed., Academic Press, New York, 1979, pp. 1–81.
- [36] L. DE ANDRADE LIMA AND A. D. REY, *Superposition principles for small amplitude oscillatory shearing of nematic mesophases*, Rheol. Acta, 45 (2006), pp. 591–600.
- [37] E. H. MACMILLAN, *A Theory of Anisotropic Fluid*, Ph.D. thesis, Department of Mechanics, University of Minnesota, Minneapolis, MN, 1987.
- [38] P. L. MAFFETTONE AND S. CRESCITELLI, *Bifurcation analysis of a molecular model for nematic polymers in shear flows*, J. Non-Newtonian Fluid Mech., 59 (1995), pp. 73–91.
- [39] P. L. MAFFETTONE, A. M. SONNET, AND E. G. VIRGA, *Shear-induced biaxiality in nematic polymers*, J. Non-Newtonian Fluid Mech., 90 (2000), pp. 283–297.
- [40] G. MARRUCCI AND F. GRECO, *The elastic constants of Maier-Saupe rodlike molecular nematics*, Mol. Cryst. Liq. Cryst., 206 (1991), pp. 17–30.
- [41] G. MARRUCCI AND F. GRECO, *Flow behavior of liquid crystalline polymers*, Adv. Chem. Phys., 86 (1993), pp. 331–404.
- [42] H. MENDIL, P. BARONI, AND L. NOIREZ, *Unexpected giant elasticity in side-chain liquid-crystal polymer melts: A new approach for the understanding of shear-induced phase transition*, Europhys. Lett., 76 (2005), pp. 983–989.
- [43] H. MENDIL, P. BARONI, AND L. NOIREZ, *Solid-like rheological response of non-entangled polymers in the molten state*, Eur. Phys. J. E, 19 (2006), pp. 77–85.
- [44] L. ONSAGER, *The effects of shape on the interaction of colloidal particles*, Ann. N. Y. Acad. Sci., 51 (1949), pp. 627–659.
- [45] C. PUJOLLE-ROBIC AND L. NOIREZ, *Observation of shear-induced nematic-isotropic transition in side-chain liquid crystal polymers*, Nature, 409 (2001), pp. 167–171.
- [46] A. D. REY AND M. M. DENN, *Dynamical phenomena in liquid-crystalline materials*, in Annual Review of Fluid Mechanics, Annu. Rev. Fluid Mech. 34, Annual Reviews, Palo Alto, CA, 2002, pp. 233–266.
- [47] G. RIENACKER, M. KROGER, AND S. HESS, *Chaotic orientational behavior of a nematic liquid crystal subjected to a steady shear flow*, Phys. Rev. E (3), 66 (2002), 040702.
- [48] L. RUSSO AND P. L. MAFFETTONE, *Nonlinear dynamics of a concentrated system of rigid rods subjected to periodic shear flow*, J. Rheol., 47 (2003), pp. 129–141.
- [49] G. SGALARI, G. L. LEAL, AND J. FENG, *The shear flow behavior of LCPs based on a generalized Doi model with distortional elasticity*, J. Non-Newtonian Fluid Mech., 102 (2002), pp. 361–382.
- [50] J. SHEN, *Efficient spectral-Galerkin method I. Direct solvers of second- and fourth-order equa-*

- tions using Legendre polynomials, *SIAM J. Sci. Comput.*, 15 (1994), pp. 1489–1505.
- [51] J. K. C. SUEN, R. NAYAK, R. C. ARMSTRONG, AND R. A. BROWN, *A wavelet-Galerkin method for simulating the Doi model with orientation-dependent rotational diffusivity*, *J. Non-Newtonian Fluid Mech.*, 114 (2003), pp. 197–228.
- [52] Z. TAN AND G. C. BERRY, *Studies on the texture of nematic solutions of rodlike polymers, 3. Rheo-optical and rheological behavior in shear*, *J. Rheol.*, 47 (2003), pp. 73–104.
- [53] T. TSUJI AND A. D. REY, *Effect of long range order on sheared liquid crystalline polymers, Part 1: Compatibility between tumbling behavior and fixed anchoring*, *J. Non-Newtonian Fluid Mech.*, 73 (1997), pp. 127–152.
- [54] T. TSUJI AND A. D. REY, *Orientation mode selection mechanisms for sheared nematic crystalline materials*, *Phys. Rev. E* (3), 57 (1998), pp. 5609–5625.
- [55] T. TSUJI AND A. D. REY, *Effect of long range order on sheared liquid crystal line materials: Flow regimes, transitions, and rheological phase diagrams*, *Phys. Rev. E* (3), 62 (2000), pp. 8141–8151.
- [56] Q. WANG, *A hydrodynamic theory of nematic liquid crystalline polymers of different configurations*, *J. Chem. Phys.*, 116 (2002), pp. 9120–9136.
- [57] Q. WANG, M. G. FOREST, AND R. ZHOU, *A hydrodynamic theory for solutions of nonhomogeneous nematic liquid crystalline polymers with density variations*, *J. Fluids Eng.*, 126 (2004), pp. 180–188.
- [58] H. YU AND P. ZHANG, *A kinetic-hydrodynamic simulation of microstructure of liquid crystal polymers in plane shear flow*, *J. Non-Newtonian Fluid Mech.*, 141 (2007), pp. 116–127.
- [59] X. ZHENG, M. G. FOREST, R. LIPTON, AND R. ZHOU, *Nematic polymer mechanics: Flow-induced anisotropy*, *Contin. Mech. Thermodyn.*, 18 (2007), pp. 377–394.
- [60] X. ZHENG, M. G. FOREST, R. LIPTON, R. ZHOU, AND Q. WANG, *Exact scaling laws for electrical conductivity properties of nematic polymer nano-composite monodomains*, *Adv. Funct. Mater.*, 15 (2005), pp. 627–638.
- [61] X. ZHENG, M. G. FOREST, R. ZHOU, R. VAIA, AND M. ARLEN, *A strategy for dimensional percolation in sheared nano-rod dispersions*, *Adv. Mater.*, 19 (2007), pp. 4038–4043.
- [62] X. ZHENG, M. G. FOREST, R. ZHOU, AND Q. WANG, *Likelihood & expected-time statistics of monodomain attractors in sheared discotic and rod-like nematic polymers*, *Rheol. Acta*, 43 (2004), pp. 17–37.
- [63] H. ZHOU AND M. G. FOREST, *Anchoring distortions coupled with plane Couette & Poiseuille flows of nematic polymers in viscous solvents: Morphology in molecular orientation, stress & flow*, *Discrete Contin. Dyn. Syst. Ser. B*, 6 (2006), pp. 407–425.
- [64] H. ZHOU AND M. G. FOREST, *Nematic liquids in weak capillary Poiseuille flow: Structure scaling laws and effective conductivity implications*, *Int. J. Numer. Anal. Model.*, 4 (2007), pp. 460–477.
- [65] H. ZHOU, M. G. FOREST, AND Q. WANG, *Anchoring-induced structure transitions of flowing nematic polymers in plane Couette cells*, *Discrete Contin. Dyn. Syst. Ser. B*, 8 (2007), pp. 707–733.
- [66] H. ZHOU, M. G. FOREST, X. ZHENG, Q. WANG, AND R. LIPTON, *Extension-enhanced conductivity of liquid crystalline polymer nano-composites*, *Macromol. Symp.*, 28 (2005), pp. 81–85.
- [67] R. ZHOU, M. G. FOREST, AND Q. WANG, *Nano-rod suspension flows: A 2D Smoluchowski-Navier-Stokes solver*, *Int. J. Numer. Anal. Model.*, 4 (2007), pp. 478–488.
- [68] R. ZHOU, M. G. FOREST, AND Q. WANG, *Kinetic structure simulations of nematic polymers in plane Couette cells. I: The algorithm and benchmarks*, *Multiscale Model. Simul.*, 3 (2005), pp. 853–870.